

RESEARCH ON NOVEL CHASSIS STRUCTURE
FOR ADVANCED MOTION CONTROL OF ELECTRIC VEHICLES

(電気自動車の運動制御のための新しい車体構造に関する研究)

THESIS

Presented to the Graduate School of
The University of Tokyo
in Partial Fulfillment
of the Requirements
for the Degree of
MASTER OF ENGINEERING
(修士学位論文)

by

YUNHA KIM
(金 潤河)

Supervisor
Professor Yoichi Hori, Ph.D.

Department of Electrical Engineering
THE UNIVERSITY OF TOKYO
August 2011

©Copyright

by

Yunha Kim

2011

to my

MOTHER and FATHER

with love

Research on Novel Chassis Structure for Advanced Motion Control of Electric Vehicles

by

YUNHA KIM

THESIS

Presented to the Graduate School of

The University of Tokyo

in Partial Fulfillment

of the Requirements

for the Degree of

MASTER OF ENGINEERING

Department of Electrical Engineering

THE UNIVERSITY OF TOKYO

August 2011

Acknowledgements

I would like to express my deep-felt gratitude to my advisor, Professor Yoichi Hori, Ph.D., of the Department of Advanced Energy at The University of Tokyo, for his advice, encouragement, patience and constant support. He always provided me with energy and clear explanations when I was lost, tired, or even doubting in my abilities. When discouraged I was always able to get refreshed by following his prescription, “Go get some drinks.” I wish all students the honor and opportunity to know him and drink with him.

I also want to thank Professor Hiroshi Fujimoto, Ph.D., Dr. Alexander Viehweider, and Dr. Sehoon Oh of the Department of Advanced Energy at The University of Tokyo, for their invaluable suggestions, comments and academic guidance. They were extremely helpful in providing expertise I needed in order to complete this work. Indeed, they are not only good instructors but also great mentors.

And I cannot thank enough Mr. Kanghyun Nam, my friend and senior student, for his invaluable help and warmest encouragements. Without his support, I would not have been able to complete this work.

Additionally, I wish to thank all the professors and staff of The University of Tokyo for their hard work and dedication, providing me the means to complete my course works and degree. Especially, Mr. Toshiyuki Uchida of the Department of Electrical Engineering at The University of Tokyo, made it possible for me to fabricate the experimental setup by providing technical suggestions and support.

For financial support, I must thank the Japanese Government, who enabled me to concentrate on studying without worrying about anything else.

And finally, I would like to thank my family for their continuing, loving support. I will never be able to express my feelings enough, only that I love you.

NOTE: This thesis was submitted to my Supervising Committee on the August 17, 2011.

Abstract

Recent popularization of electric vehicles is remarkable. Some of the leading automobile manufacturers are launching partially or fully electrified vehicles to compete for the pre-occupancy of the market, and many research groups around the world are working on the vehicle electrification and its related issues. Also each of the governments all over the world is planning the country's transportation electrification target, which is expected to be sharply increasing in the near future.

One of the major reasons for the recent revisiting of EVs is the increasing concern for the environmental issues. EVs are zero-emission vehicles, which means that they do not emit carbon oxides, nitrogen oxides, and carbon hydrates, which are known to be causing environmental problems. In addition, but more important point is that EVs are said to be more energy efficient than the conventional internal combustion engine vehicles. The well-to-wheel efficiency of EVs is fairly comparable to that of ICEVs, however, the price is much cheaper, and the tank-to-wheel efficiency of EVs overwhelms that of ICEVs.

However, the merits of the vehicle electrification do not remain only in the environmental or energy perspectives. By using electric motors in the drivetrain, the vehicle motion control can be changed. From the motion control point of view, it is widely known that, compared to conventional vehicles mounting internal combustion engines, electric vehicles have several significant advantages in vehicle dynamic performance for the sake of the excellence of electric motors in control.

Utilizing the advantages of using electric motor, many motion control strategies for EVs, such as anti-slip traction control, and roll and yaw stability control, are introduced. These control methods turned out to be reasonably effective that EVs can run more safely than the ICEVs in poor road conditions. In addition to these properties, vehicle electrification enables EVs to excel the conventional ICEVs in terms of vehicle motion, by assigning EVs two kinds of inputs – the steering and the direct yaw moment – while the conventional

vehicles have only one input – the steering.

However, most of these research works are based on the four-wheeled vehicle chassis structure with the conventional mechanical steering system, which has not been changed from the beginning of the massive production of the Ford Model T in 1908. It is originally designed and optimized for an internal combustion engine to transmit all power to the four driving wheels. Consequently it is clear that to use the conventional chassis structure for the independent motor driven EVs is a waste of ability, which is the motivation for this thesis. This thesis is on the study and proposal of a novel structure of EVs for advanced motion control.

Despite the underlying importance, however, it seems that there has been no attempt to provide an appropriate and unique structure for the independent motor driven EVs. In this work, followed by the studies on wheel placements and their effects on the vehicle behavior, a novel chassis structure using caster wheels and independent driving motors is proposed. Provided with four wheels the system is designed to be statically stable, and with caster wheels on the front axle the proposed system is able to use the two kinds inputs – the steering and the direct yaw moment – effectively for two-dimensional motion control.

The consequent unique advantages of the system are shown with experimental results. Considering the advantages shown in this work, the proposed system could be an attractive alternative for the future EV's structure for better dynamic performances.

This thesis first introduces the background and the motivation of the work in chapter 1, and covers the fundamentals of vehicle dynamics in chapter 2, which underlie the observations and discussions throughout this work. In chapter 3, wheel placements and their effects on the vehicle dynamics are studied. Some criteria to evaluate the system stability and compatibility are introduced and used, and the results of the evaluations are discussed. Based on the study, a novel structure for EVs using caster wheels and independent driving motors is proposed in chapter 4. The system is analyzed with its corresponding mathematical model, and the advantages of the system are shown with the experimental results. Finally, conclusive remarks are made, and future works are shown in chapter 5.

Table of Contents

	Page
Acknowledgements	v
Abstract	vi
Table of Contents	viii
Chapter	
1 Introduction	1
1.1 Background	1
1.2 Outline	5
2 Vehicle Dynamics	6
2.1 Lumped Mass and Coordinate Convention	6
2.2 Mechanics of Tire Force Generation	7
2.2.1 Longitudinal Force Generation	8
2.2.2 Lateral Force Generation	10
2.2.3 Maximum Friction Circle	11
2.3 Steering and Cornering	12
2.3.1 Low Speed Turning	13
2.3.2 High Speed Turning	15
2.3.3 Side Slip Angle	19
2.4 Two-Dimensional Vehicle Dynamics	20
2.5 Summary	20
3 Study on Wheel Placements	22
3.1 Introduction	22
3.2 Wheel Placements and Corresponding Models	22
3.2.1 Two-Wheeled Vehicle and its Dynamics	23
3.2.2 Three-Wheeled Vehicle and its Dynamics	27

3.2.3	Four-Wheeled Vehicle and its Dynamics	30
3.3	Structural Stability Evaluation	31
3.3.1	Static Stability Factor (SSF)	33
3.3.2	Load Transfer Metric (LTM)	34
3.3.3	Energy Stability Margin (ESM)	35
3.3.4	Force-Angle Stability Metric (FAS)	36
3.4	Study on Compatibility with EV Motion Control	40
3.4.1	Controllability	40
3.4.2	Steering Input and Vehicle Yaw Response	42
3.4.3	Direct Yaw Moment Input and Vehicle Yaw Response	43
3.5	Summary	45
4	A Novel Chassis Structure for EVs using Caster Wheels and Independent Driving Motors	47
4.1	Introduction	47
4.2	Caster Wheels and Vehicle Dynamics	48
4.3	Experimental Vehicle and its Modeling	50
4.3.1	Consideration of Wheel Placement	50
4.3.2	Experimental Vehicle, CIMEV	55
4.3.3	Mathematical Modeling	57
4.4	System Analyses of CIMEV	62
4.4.1	Stability Analysis	62
4.4.2	Controllability Analysis	64
4.4.3	System Yaw Response	66
4.5	Controller Design	67
4.5.1	Upper-level Controller	68
4.5.2	Driving Controller	69
4.5.3	Steering Controller and Lateral Force Observer	70
4.5.4	Speed Range and Control Mode	71

4.6	Experiment Results and Advantages of CIMEV	72
4.6.1	High Mobility at Low Speed	72
4.6.2	Making Use of Lateral Force Observer	74
4.7	Summary	81
5	Concluding Remarks	83
5.1	Significance of the Result	83
5.2	Future Works	83
	References	85
	Curriculum Vitae	89

Chapter 1

Introduction

1.1 Background

Recent popularization of electric vehicles (EVs) is remarkable. Some of the leading automobile manufacturers are launching partially or fully electrified vehicles to compete for the preoccupancy of the market (see Figure 1.1), and many research groups around the world are working on the vehicle electrification and its related issues. Also each of the governments all over the world is planning the country's transportation electrification target, which is expected to be sharply increasing in the near future as shown in Fig. 1.2.

The attempt to propagate EVs, however, is not the first time in history. Thomas Davenport built an EV for the first time in 1835, and Robert Davidson made an electric locomotive to attain a speed of 6 km/h [1]. In 1830s, Robert Anderson invented the first electric carriage using non-rechargeable primary cells [2]. By the 20th century, electrified vehicles have become widely used in many industrial fields, such as railway transportations,



Figure 1.1: Toyota's Prius(left) and Mitsubishi's i-MiEV(right)

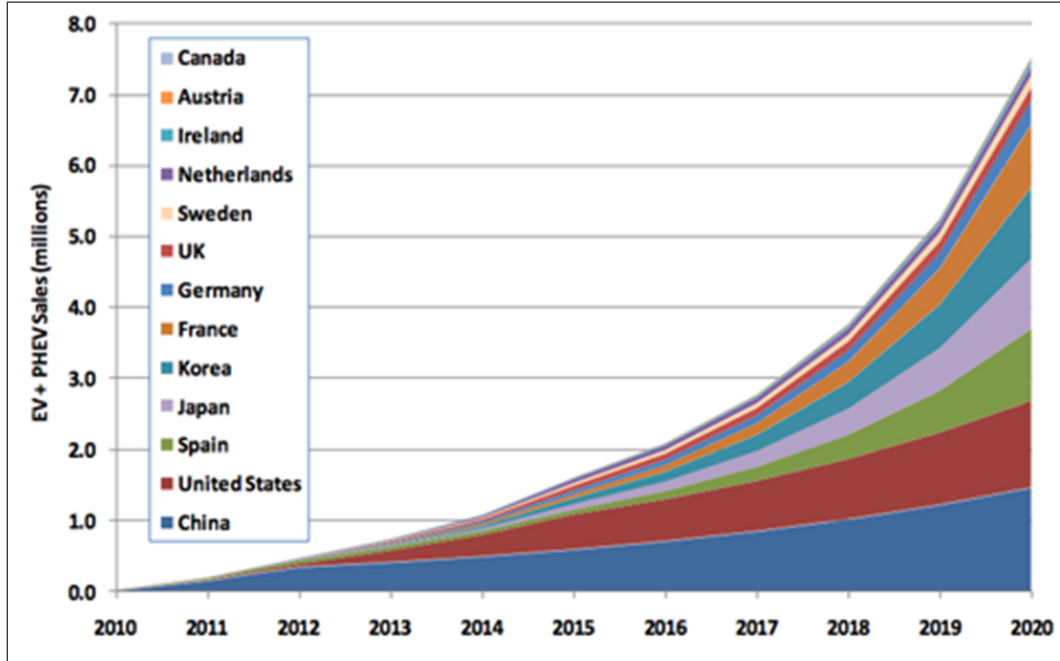


Figure 1.2: Slide from IEA presentation showing project sales of electric and plug-in hybrid sales through 2020.

indoor locomotions, and many other applications [3]. Electric vehicles are the earliest form of automobiles and have played a great role in transportation, however, for the sake of the powerful internal combustion engines, they have been hardly seen on the roads. Now they revisited.

One of the major reasons for the recent revisiting of EVs is the increasing concern for the environmental issues. Electric vehicles are practically zero-emission vehicles (ZEVs), which means that they do not emit carbon oxides, nitrogen oxides, and carbon hydrates, which are known to be causing several environmental problems. In addition to this, but more important point is that EVs are said to be more energy efficient than the conventional internal combustion engine vehicles (ICEVs). The well-to-wheel efficiency of EVs is fairly comparable to that of ICEVs, however, the price is much cheaper – about 17% of gasoline, and the tank-to-wheel efficiency of EVs (around 90%) overwhelms that of ICEVs (around 30%) [4][5].

Thus many of the researchers are focusing on the energy managing systems involving batteries, capacitors, or fuel cells for instance [6]. Some of them are into charging and power transfer techniques [7][8], and many others are focusing on the infrastructural studies.

However, the merits of the vehicle electrification do not remain only in the environmental or energy perspectives. By using electric motors in the drivetrain, the vehicle motion control can be changed. From the motion control point of view, it is widely known that, compared to conventional vehicles mounting internal combustion engines, electric vehicles have several significant advantages in vehicle dynamic performance such as [9]:

- electric motors have very quick torque response (1ms or less);
- electric motors have highly accurate output torque;
- there is no difference between acceleration and deceleration (i.e. electric motors act as both engine and brake);
- electric motors are compact so that they can be fitted in each wheel (In-Wheel Motor: IWM (See Fig.1.3));

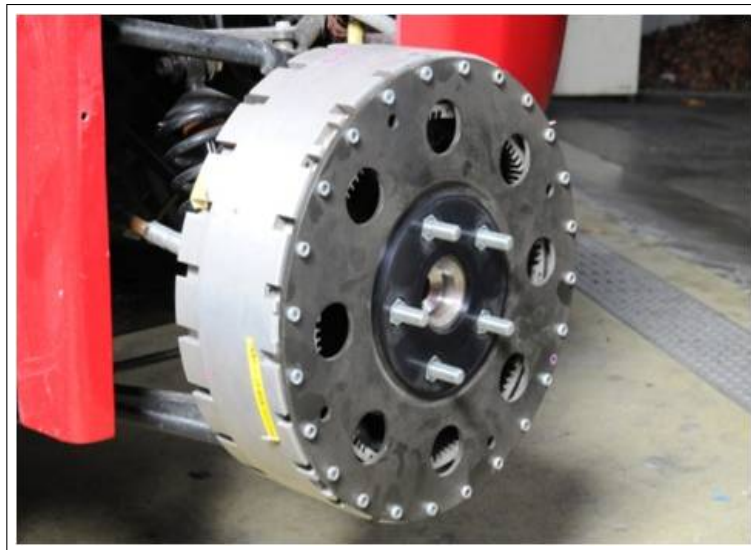


Figure 1.3: An In-Wheel Motor.



Figure 1.4: Ford Model T in 1908.

- and the motor torque can be measured easily.

Utilizing these advantages of using electric motor, many motion control strategies for EVs, such as anti-slip traction control [10], and roll and yaw stability control [11], are introduced. These control methods turned out to be reasonably effective that EVs can run more safely than the ICEVs in poor road conditions. In addition to these properties, vehicle electrification enables EVs to excel the conventional ICEVs in terms of vehicle motion, by assigning EVs two kinds of inputs – the steering and the direct yaw moment – while the conventional vehicles have only one input – the steering.

However, most of these research works are based on the four-wheeled vehicle chassis structure with the conventional mechanical steering system, which has not been changed from the beginning of the massive production of the Ford Model T in 1908 (Fig. 1.4). It is originally designed and optimized for an internal combustion engine to transmit all power to the four driving wheels. Consequently it is clear that to use the conventional chassis structure for the independent motor driven EVs is a waste of ability, which is the motivation for this thesis. This thesis is on the study and proposal of a novel structure of EVs for advanced motion control.

1.2 Outline

This thesis first covers the fundamentals of vehicle dynamics in chapter 2, which underlie the observations and discussions throughout this work. In chapter 3, wheel placements and their effects on the vehicle dynamics are studied. Some criteria to evaluate the system stability and compatibility are introduced and used, and the results of the evaluations are discussed. Based on the study, a novel structure for EVs using caster wheels and independent driving motors is proposed in chapter 4. The system is analyzed with its corresponding mathematical model, and the advantages of the system are shown with the experimental results. Finally, conclusive remarks are made, and future works are shown in chapter 5.

Chapter 2

Vehicle Dynamics

Vehicle dynamics is concerned with the movements of vehicles on a road surface. The dynamic behavior of a vehicle is determined by the forces and moments acting on the vehicle generated from the tires, gravity, and aerodynamics. The vehicle dynamics is studied to determine what forces and moments will be produced by each of components under a particular condition, and how the vehicle will respond to these forces and moments. The movements of interest in this paper are mainly ride and cornering, and thus it is essential to cover the systems and the conventions that will be used to describe these motions. In the following sections, the lumped mass assumption, the coordinate systems, and the dynamics of the tire force, the steering and cornering, and the vehicle yaw will be explained.

2.1 Lumped Mass and Coordinate Convention

An automobile is made up of many – usually more than 20,000 – components assembled within its body. For many of the dynamic analyses, however, it is assumed that all parts move together as a rigid body; thus it can be represented as one lumped mass located at its center of gravity (CG). In this paper, it is assumed that the vehicle is reasonably rigid, and thus has its mass concentrated at CG, with the equivalent rotational moments of inertia.

In order to describe the on-board vehicle motion, the vehicle fixed coordinate system, defined as follows, is used throughout the paper (Fig. 2.1). By this convention, the coordinates are:

x : Forward and on the longitudinal plane of symmetry

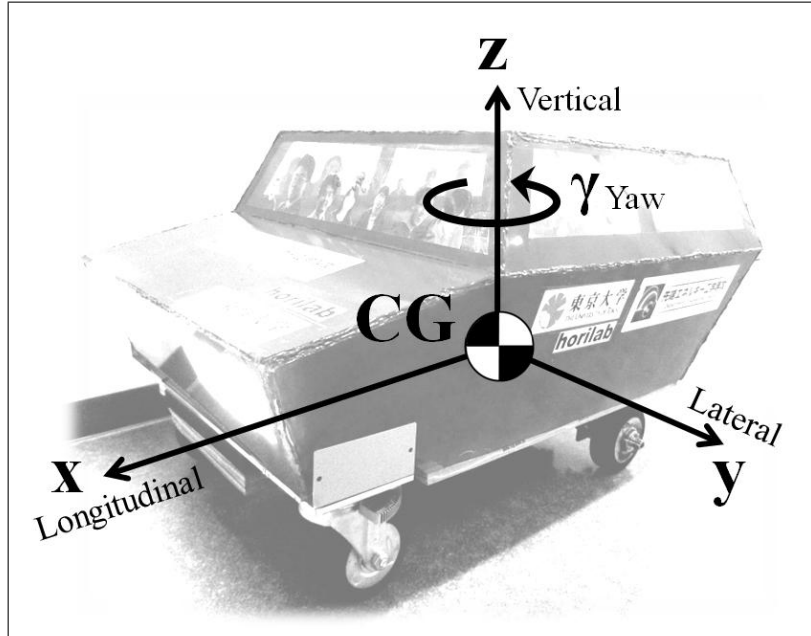


Figure 2.1: Vehicle Fixed Coordinate System.

y : Lateral out the left side of the vehicle

z : Upward with respect to the vehicle

γ : Yaw velocity about the z axis

2.2 Mechanics of Tire Force Generation

Most of all the forces which are applied to the vehicle are generated in the tire-road interface. It has been said that “the critical control forces that determine how a vehicle turns, brakes, and accelerates are developed in four contact patches no bigger than a man’s hand.” Thus it is essential to understand the mechanism of the tire force generation for explaining the vehicle dynamics. The tire serves essentially three basic functions [12]:

- It supports the vertical load, while cushioning against road shocks.
- It develops longitudinal forces for acceleration and braking.

- It develops lateral forces for cornering.

While the tire seems to be a simple rubber toroid, it is, however, a very complex non-linear system which is difficult and complex to quantify. Many simplified tire models have been introduced to approximate the tire behaviors, but for the purpose of understanding their role in the vehicle dynamics it is sufficient to review empirical data which shows its essential properties. Among the aforementioned basic functions, the latter two, which are of our particular interest, are shown in this paper.

2.2.1 Longitudinal Force Generation

Fig.2.2 (a) shows a tire and the forces imposed on it when the vehicle runs on a flat road. This motion can be described with the following equations:

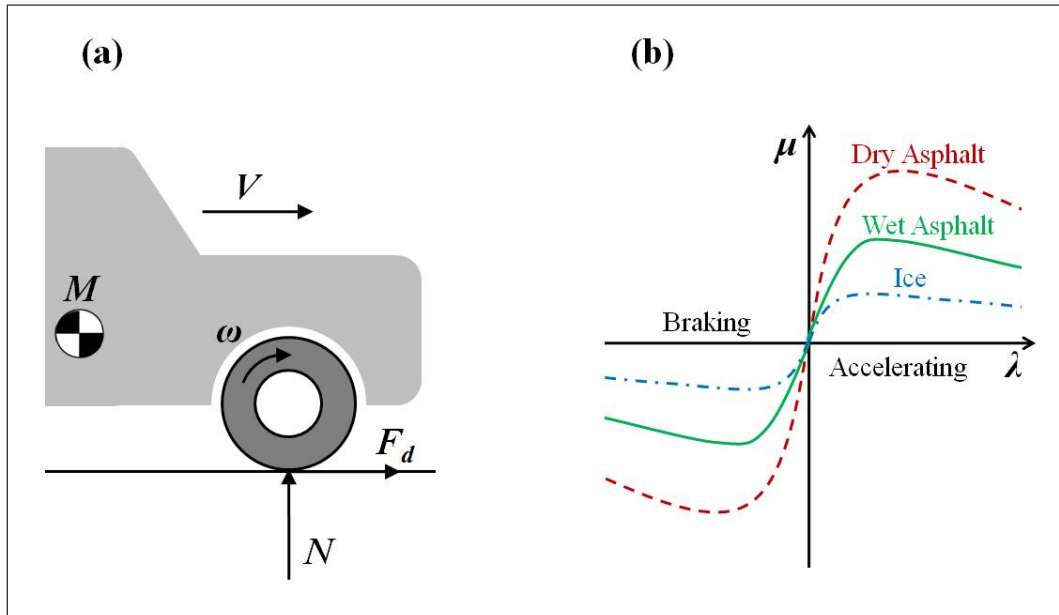


Figure 2.2: One wheel model of a vehicle on a flat road(a), and the μ - curve on different road surfaces(b).

$$M\dot{V} = F_d(\lambda) = N\mu(\lambda) \quad (2.1)$$

$$I_w\dot{\omega} = T_m - rF_d(\lambda) \quad (2.2)$$

$$V_w = r\omega \quad (2.3)$$

$$\lambda = \frac{V_w - V}{\max(V_w, V)} \quad (2.4)$$

where,

M : the lumped mass of the vehicle;

I_w : the moment of inertia of the wheel;

V : the vehicle speed;

r : the wheel radius;

ω : the rotational speed of the wheel;

T_m : the driving motor torque;

F_d : the driving force exerted on the tire-road interface;

N : the tire normal force; and

λ : the slip ratio.

The driving force F_d is a function of the slip ratio. Because the driving force is essentially the friction force between the tire and the road, and the slip ratio and the friction are related in the way shown in Fig.2.2 (b). Where μ here is the tire friction force normalized by the tire normal force N . When λ is small enough μ seems to be linear to λ . Typically the friction force will reach the maximum when the slip ratio approaches 0.15~0.2 on the asphalt, and 0.1 or below on an icy road, where the maximum friction force will be generally in the range of 70~90% of the tire normal force on a dry asphalt, 25~50% on a wet asphalt, and 10~15% on an icy road.

2.2.2 Lateral Force Generation

To develop the lateral forces is one of the most important functions of a tire. Because the lateral forces are essential to control the direction of the vehicle, generate lateral acceleration during cornering, and resist external disturbances such as wind and cross-slope. These lateral forces are mainly generated by the lateral slip of the tire.

When a tire is rolling, if there exist some discrepancy in angle between the direction of travel and the tire heading, the tire is subjected to a lateral force. This angle is called the tire slip angle α . As it can be seen in Fig.2.3, the lateral force is distributed within the contact patch in a way it has a peak at the point that the friction force equals the lateral force. Generally the lateral force refers to the net force F_y , whose acting point is usually behind the center of z -directional rotation, which results in the self-aligning moment M_{sa} . The distance between the acting point and the center of z -directional rotation is called the pneumatic trail. The magnitude of the self-aligning moment is equal to the lateral force times the pneumatic trail.

The lateral force F_y and the self-aligning moment M_{sa} are commonly expressed as empirical models of the tire slip angle α at steady state turning. Experimental measurements show the characteristic relationship to slip angle in the way shown in Fig.2.4. The most important property of the turning and stability behavior of a vehicle is the initial slope of the lateral force curve, which is known as “the cornering stiffness”, C_f for front wheels, and C_r for rear wheels. These parameters are defined as follows (The lateral forces are denoted here as Y_F for the front and Y_R for the rear.):

$$C_f = \left. \frac{\partial Y_F}{\partial \alpha_f} \right|_{\alpha_f=0} \quad (2.5)$$

for front wheels and

$$C_r = \left. \frac{\partial Y_R}{\partial \alpha_r} \right|_{\alpha_r=0} \quad (2.6)$$

for rear wheels.

The cornering stiffness is dependent on many variables, such as tire size, construction type, width, tread, and etc.. However for a given tire, the vertical load N is the dominant factor. In addition, vehicle speed does not strongly influence the cornering forces produced by a tire.

2.2.3 Maximum Friction Circle

The longitudinal and the lateral tire forces are essentially the friction forces generated from the tire-road interface. Thus the vector sum of the two has the limit in its magnitude, which is generally circular in shape. This circle is called “the maximum friction circle,” which is shown in Fig.2.5. In addition, Fig.2.6 shows the relationship between the longitudinal force and the self-aligning moment which is also bounded by the friction limit of the tire-road interface. The individual curves represent the lateral force or the self-aligning moment at a given slip angle.

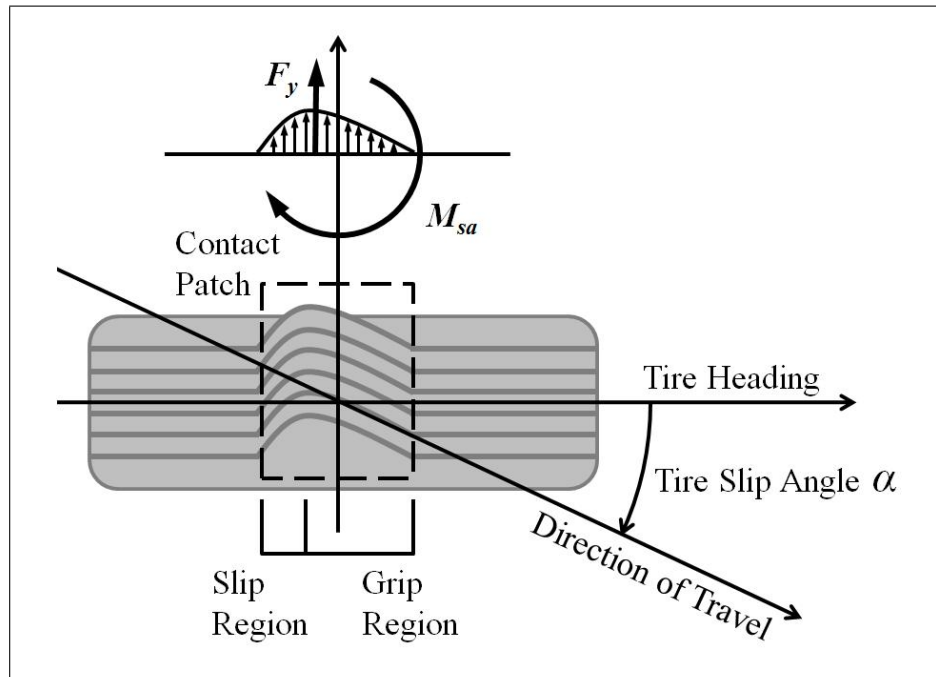


Figure 2.3: Tire deformation and lateral force generation.

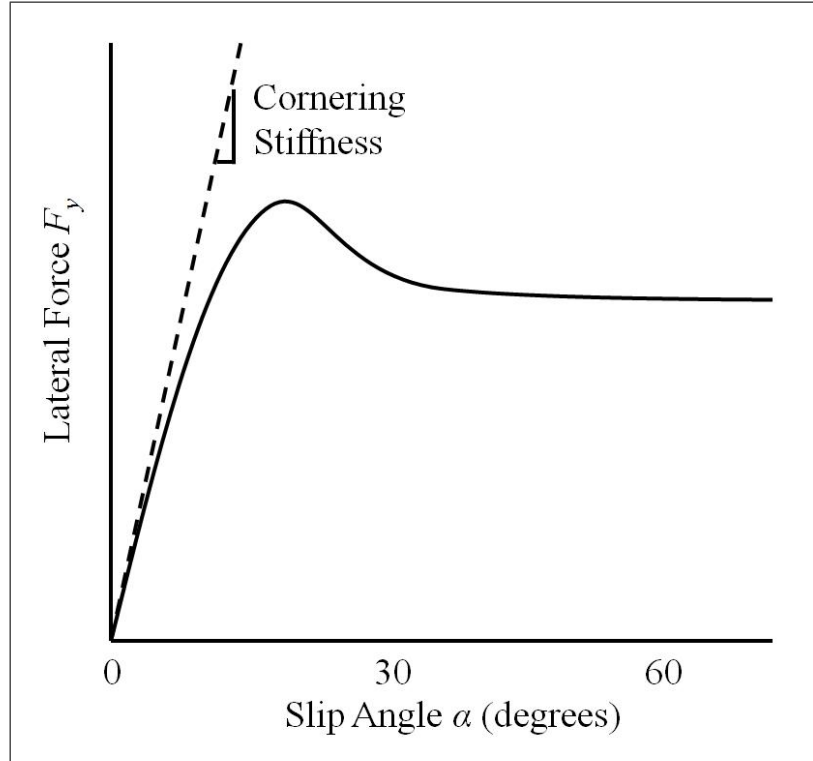


Figure 2.4: Tire lateral force properties.

The vector sum of the tire forces can not exceed the friction limit. (Although there are some tires optimized for lateral traction or braking traction, in which case the limit is an intended ellipse.) Otherwise the tire loses its grip on the road. It is worth noting that the friction limit for a tire, regardless of direction, is determined by the coefficient of friction times the vertical load.

2.3 Steering and Cornering

The cornering behavior of a vehicle is an important performance index, which involves vehicle-driver combination. The vehicle-driver combination is a closed-loop system – meaning that the driver is a sort of feedback controller, however, for characterizing only the vehicle, usually open-loop behavior is analyzed. Open-loop refers to vehicle response to

specific steering inputs, and is more precisely defined as “directional response” behavior. In this section open-loop cornering, or directional response behavior, will be introduced.

2.3.1 Low Speed Turning

At low vehicle speed, the tire does not develop lateral forces, i.e. they roll with no slip angle. Thus the motion of the vehicle is defined only by the geometry of the wheels, shown in Fig.2.7. Since there is no slip angle in rear wheels, the center of turning lies on the projection of the rear axle. Similarly, the perpendicular from each of the front wheels passes through the center of turning. In this way the ideal steering angles of the front wheels are established. Assuming small angles, the steer angles are given as:

$$\delta_L = \arctan \frac{L}{R - \frac{d}{2}} \simeq \frac{L}{R - \frac{d}{2}} \quad (2.7)$$

$$\delta_R = \arctan \frac{L}{R + \frac{d}{2}} \simeq \frac{L}{R + \frac{d}{2}} \quad (2.8)$$

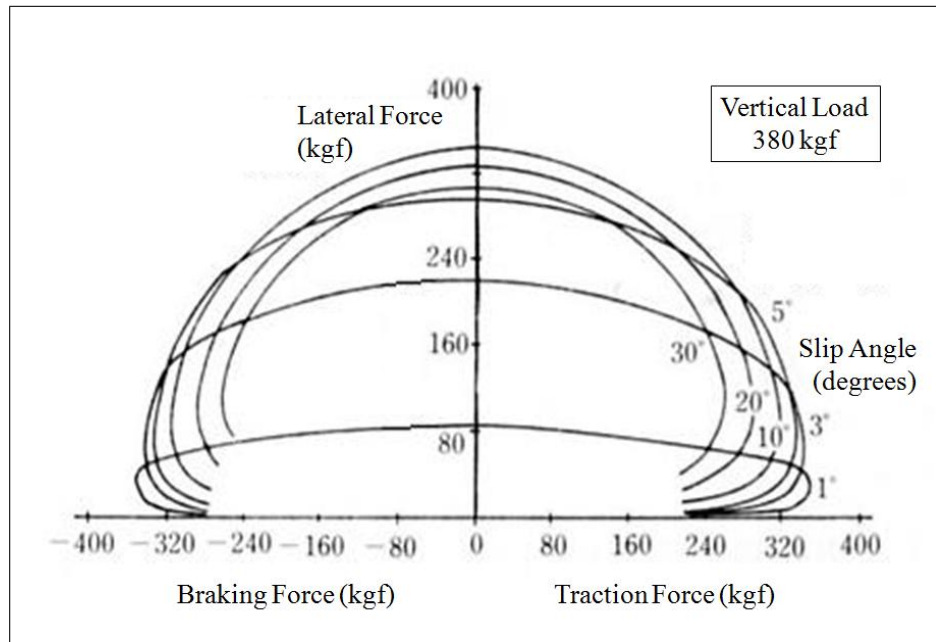


Figure 2.5: Longitudinal force and lateral force [13].

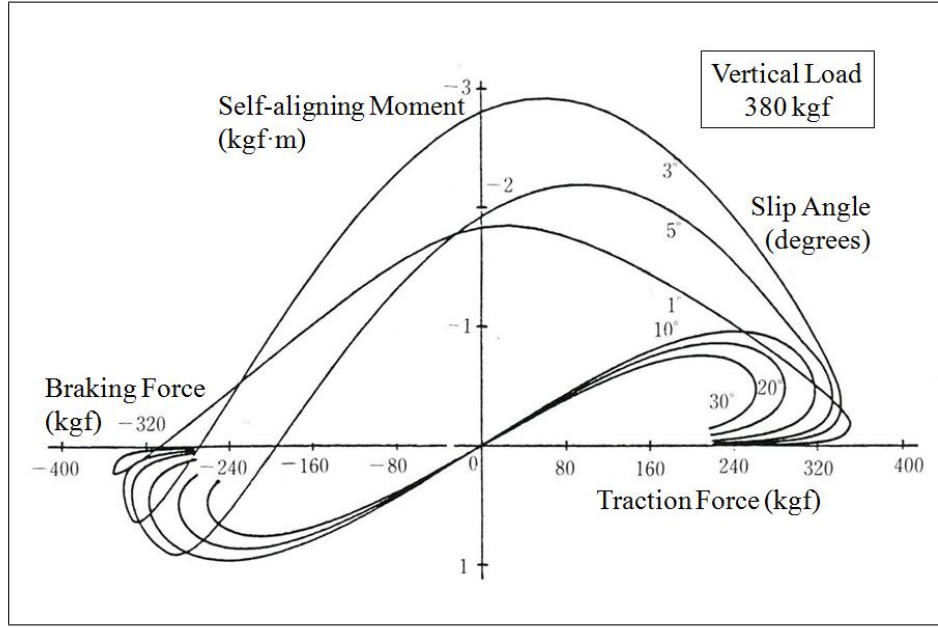


Figure 2.6: Longitudinal force and self-aligning moment [13].

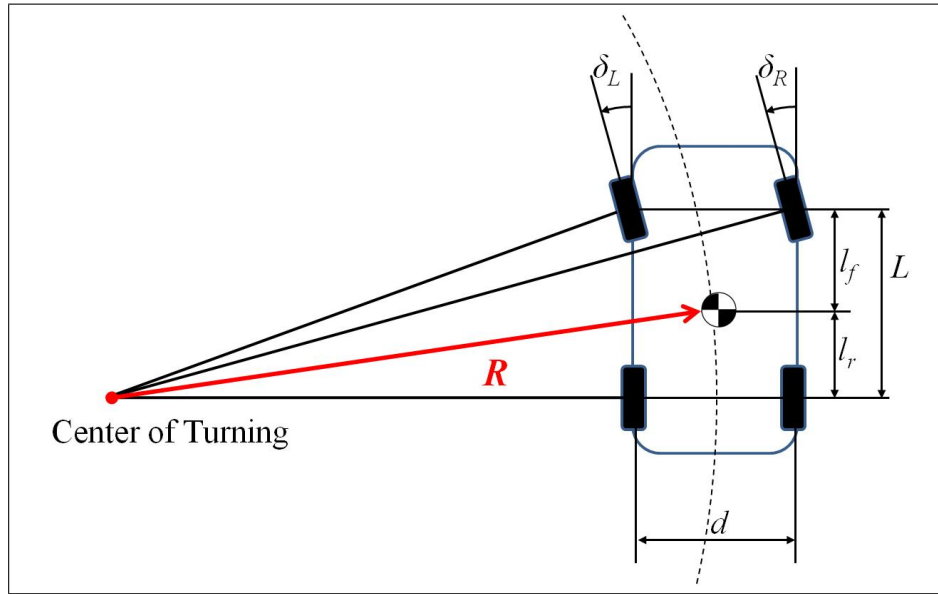


Figure 2.7: Geometry of a turning vehicle at low speed.

where, δ_L , δ_R are the steering angles of the inner and outer wheels, the left and right wheels in the case above, respectively.

The average angle of the front wheels is defined as the Ackermann Angle [14]:

$$\delta_A = \frac{L}{R} \quad (2.9)$$

The Ackermann Geometry is generally used for describing the exact geometry of the front wheels shown in Fig.2.7. With this geometry, the steering torque tends to increase with increasing steering angle, which provides the driver with a natural feel in the feedback through the steering wheel.

2.3.2 High Speed Turning

When a vehicle is turning at high speed, centrifugal acceleration will be present. To counteract the lateral acceleration the tires develop lateral forces, thus slip angles α are present at each wheel.

The lateral forces Y_F and Y_R , are called the “cornering forces” when the camber angle is zero. Assuming small slip angles — usually 5 degrees or less, the relationship between the slip angle and the lateral force is regarded as linear (See Fig.2.4), thus the cornering forces are defined as follows:

$$Y_F = C_f \alpha_f \quad (2.10)$$

$$Y_R = C_r \alpha_r \quad (2.11)$$

where C_f and C_r are the cornering stiffness defined by equations (2.5) and (2.6), respectively. Using the bicycle model with these equations, the steady state cornering of a vehicle can be described as follows:

$$\Sigma F_y = Y_F + Y_R = \frac{mV^2}{R} \quad (2.12)$$

$$Y_F l_f - Y_R l_r = 0 \quad (2.13)$$

where,

m : Mass of the vehicle,

V : Longitudinal velocity of the vehicle,

R : Radius of the turn,

l_f : Distance between the center of gravity and the front axle, and

l_r : Distance between the center of gravity and the rear axle.

Substituting equation (2.13) into (2.12) yields:

$$Y_F = \frac{l_r MV^2}{RL} \quad (2.14)$$

$$Y_R = \frac{l_f MV^2}{RL} \quad (2.15)$$

With the required lateral forces known, the slip angles at the front and rear wheels can be calculated from equations (2.10) and (2.11). That is:

$$\alpha_f = \frac{l_r m V^2}{C_f RL} \quad (2.16)$$

$$\alpha_r = \frac{l_f m V^2}{C_r RL} \quad (2.17)$$

With this calculation, the description of the geometry shown in Fig.2.7 can be modified as follows:

$$\delta = \delta_A + \alpha_f - \alpha_r = \frac{L}{R} + \frac{l_r m V^2}{C_f RL} - \frac{l_f m V^2}{C_r RL} \quad (2.18)$$

Taking into account the following kinematics concerning the tire normal forces acting on the front axle N_f and the rear N_r :

$$N_f = \frac{l_r mg}{L} \quad (2.19)$$

$$N_r = \frac{l_f mg}{L} \quad (2.20)$$

Equation (2.18) can be rewritten as:

$$\delta = \frac{L}{R} + \left(\frac{N_f}{C_f} - \frac{N_r}{C_r} \right) \frac{V^2}{gR} \quad (2.21)$$

This equation is often written in a short form as follows:

$$\delta = \frac{L}{R} + K_{us}a_y \quad (2.22)$$

where,

K_{us} : Understeer gradient (rad/g)

a_y : Lateral acceleration (g)

The term $\left(\frac{N_f}{C_f} - \frac{N_r}{C_r} \right)$ or K_{us} determines the magnitude and the direction of the steering input required. It is generally called the “Understeer Gradient.” With regard to this criterion, there are three cases: Neutral Steer, Understeer, and Oversteer.

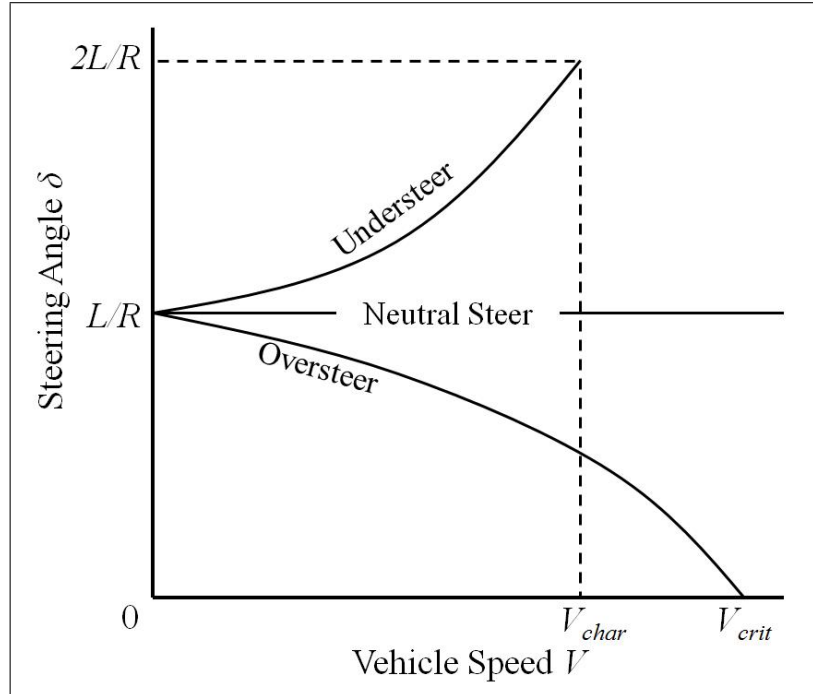


Figure 2.8: Change of steer angle with speed.

Neutral Steer(NS) In case that $\frac{N_f}{C_f} = \frac{N_r}{C_r}$ or $K_{us} = 0$, on a constant radius turn, there will be no change in steer angle with respect to the change in vehicle speed. Specifically, the steer angle required to maintain the turn will be equivalent to the Ackermann Angle δ_A .

Understeer(US) In case that $\frac{N_f}{C_f} > \frac{N_r}{C_r}$ or $K_{us} > 0$, on a constant radius turn, the steer angle has to increase with vehicle speed to maintain the turn. Usually, passenger vehicles are designed to have understeer characteristics in order to achieve steering stability at high speed. The understeer level can be quantified by the characteristic speed [15]. Characteristic speed is defined as the speed at which the steer angle required to maintain the turn is twice the Ackermann Angle, which can be calculated as:

$$V_{char} = \sqrt{\frac{Lg}{K_{us}}} \quad (2.23)$$

Oversteer(OS) In case that $\frac{N_f}{C_f} < \frac{N_r}{C_r}$ or $K_{us} < 0$, on a constant radius turn, the steer angle has to decrease as the vehicle speed is increased. The outward drift at the rear wheels turns the vehicle inward diminishing the radius of the turn. The vehicle easily gets directionally unstable with oversteer characteristics at high speed. This is called the critical speed, which is given by:

$$V_{crit} = \sqrt{-\frac{Lg}{K_{us}}} \quad (2.24)$$

These steering characteristics are indicated in Fig.2.8.

In addition, one of the main purposes of steering is to change the heading angle of a vehicle by developing the yaw rate or the yaw velocity. By considering the yaw rate γ and the yaw velocity gain $\frac{\gamma}{\delta}$, which are defined as:

$$\gamma = \frac{V}{R} \quad (2.25)$$

$$\frac{\gamma}{\delta} = \frac{V/L}{1 + \frac{K_{us}V^2}{Lg}} \quad (2.26)$$

the steering characteristics can be redrawn as Fig.2.9.

2.3.3 Side Slip Angle

At any point on the vehicle during cornering, the angle between the longitudinal axis x and the local direction of travel is called the side slip angle. In general, the side slip angle of a turning vehicle is defined at the center of gravity of the vehicle, and denoted as β . For any speed the side slip angle β is:

$$\beta = \frac{l_r}{R} - \alpha_r = \frac{l_r}{R} - \frac{N_r V^2}{C_r g R} \quad (2.27)$$

By using the side slip angle, the longitudinal V_x and the lateral speed V_y of a turning vehicle can be approximated as follows:

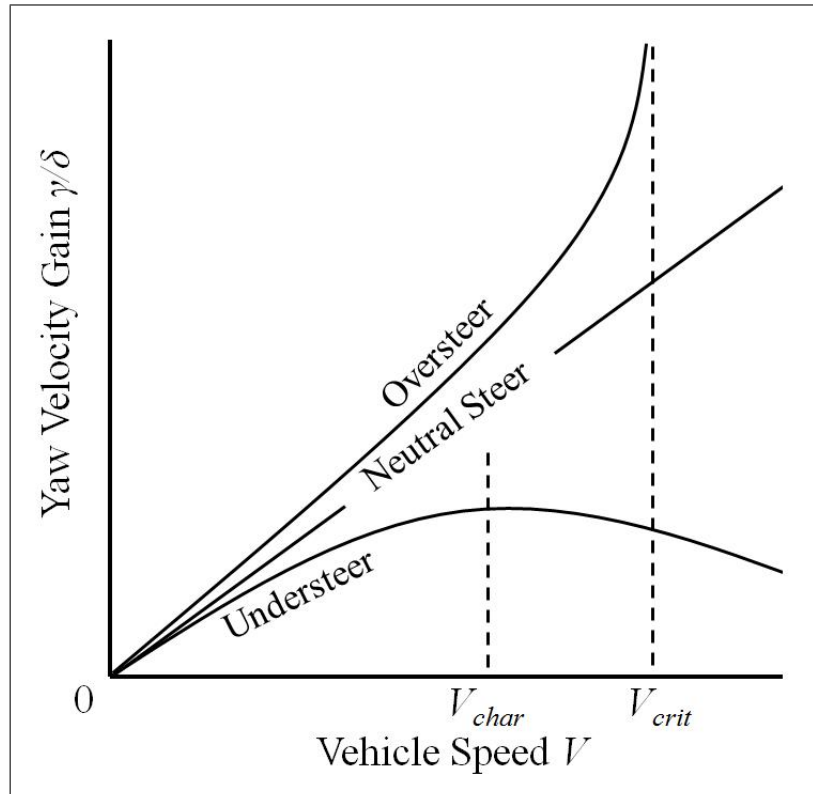


Figure 2.9: Yaw velocity gain change with speed.

$$V_x = V \cos \beta \simeq V \quad (2.28)$$

$$V_y = V \sin \beta \simeq V\beta \quad (2.29)$$

Moreover, since we are using the vehicle-fixed coordinates, the longitudinal a_x and the lateral acceleration a_y of a turning vehicle at a constant speed can be expressed as:

$$a_x = -V(\dot{\beta} + \gamma)\beta \quad (2.30)$$

$$a_y = V(\dot{\beta} + \gamma) \quad (2.31)$$

2.4 Two-Dimensional Vehicle Dynamics

Based on the mechanisms explained in previous sections, two-dimensional vehicle dynamics can be described as follows:

$$ma_y = 2Y_F + 2Y_R \quad (2.32)$$

$$I_z \dot{\gamma} = 2l_f Y_F - 2l_r Y_R + M_z \quad (2.33)$$

where,

I_z : Moment of inertia of the vehicle, and

M_z : Direct yaw moment input from the differential torque of the driving motors.

Equation (2.32) accounts for the equilibrium of the forces, and equation (2.33) for the equilibrium of the moments during cornering. Note that the four wheel vehicle model is used here.

2.5 Summary

In this chapter, the lumped mass assumption, the coordinate systems, and the dynamics of the tire force generation, the steering and cornering behavior, and the vehicle yaw dynamics

were explained. The equations introduced here will be used and referred to throughout the thesis.

Chapter 3

Study on Wheel Placements

3.1 Introduction

In order to find out a novel chassis structure which is the most appropriate for an independent-motor-driven EVs, it is necessary to discuss the wheel placements and their effects on the vehicle behavior. In this chapter, various wheel placements are considered and assessed with some vehicle stability evaluation criteria to see the compatibility with the view point of EV motion control. In the following sections, various wheel placements and corresponding dynamics will be introduced and the stability evaluation criteria are shown, and the discussion on the compatibility with the EV motion control follows.

3.2 Wheel Placements and Corresponding Models

In this section four kinds of vehicle wheel placements and their dynamics are introduced (See Fig.3.1). In the following subsections, two-wheeled vehicle dynamics, three-wheeled vehicle dynamics with one wheel front, three-wheeled vehicle dynamics with one wheel rear, and four-wheeled vehicle dynamics will be introduced in order. It is assumed that each of the dynamic models has two independent driving motors in the system, and the effect of the suspension system is ignored.

Major assumptions for the system analyses are as follows:

Assumption 1 *All vehicle models introduced in this chapter share the parameters below in Table 3.1, which are equivalent to those of CIMEV (Fig. 4.4).*

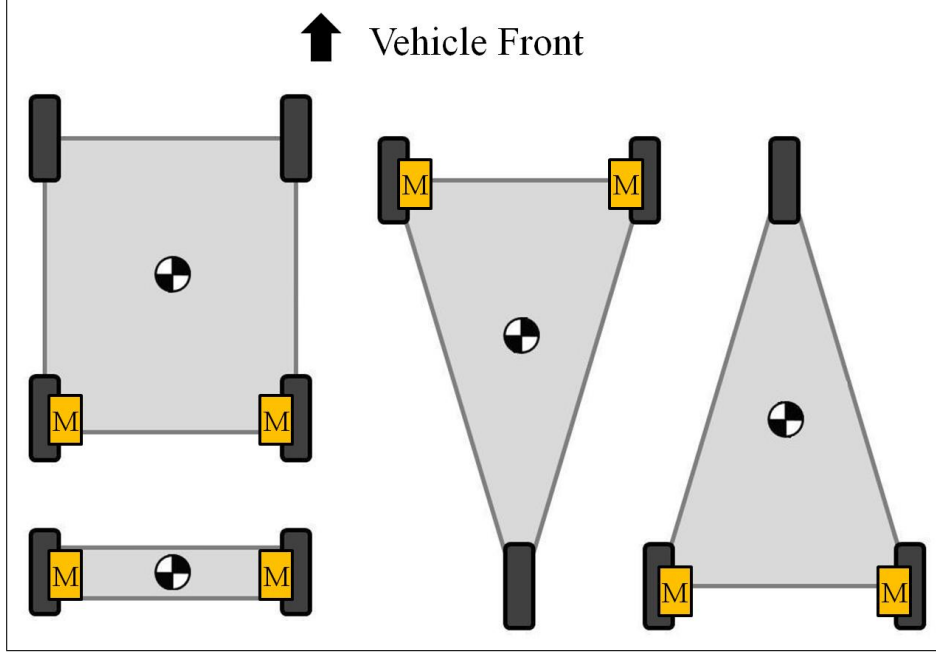


Figure 3.1: Vehicle models of consideration. The gray colored area represents the base, and the yellow boxes marked with ‘M’ indicate the independent driving motors.

Assumption 2 *Each system has two independent driving motors within it, and the steering wheels are on the front.*

Assumption 3 *The effect of the suspension system on the vehicle dynamics is ignored.*

Assumption 4 *The center of gravity of each system is assumed to be located at its geometric center of the base, i.e. each wheel negotiates with equally divided vertical load.*

3.2.1 Two-Wheeled Vehicle and its Dynamics

There have been many studies on the analyses of two-wheeled vehicle dynamics. Most of them are about motorcycles, whose wheels are in tandem. Applying independent driving motors to motorcycles, however, does not make any change in the traction distribution compared to the ICE-driven ones; therefore it is not of our interest.

Table 3.1: Common Parameter Assumptions

Parameters	Meanings	Values	Units
m	Vehicle mass	18.5	kg
I_x	Moment of inertia (x-direction)	0.250	kgm^2
I_z	Moment of inertia (z-direction)	0.409	kgm^2
C_f, C_r	Cornering stiffness	$2.86N_z$	N/rad
N_z	Vertical load	181.5/Number of wheels	N
l_f	Distance, C.G. to front axle	According to geometry	m
l_r	Distance, C.G. to rear axle	According to geometry	m
h	Distance, C.G. to road surface	0.16	m
L	Wheel base	0.435	m
d	Tire track	0.355	m
R	Tire radius	0.05	m
δ	Steering angle of the steering wheel	—	rad
M_z	Direct yaw moment input	—	Nm

Some studies on Segway (Fig. 3.2) — a two-wheeled, self-balancing electric vehicle invented by Dean Kamen — are shown here. Two wheels are attached transversely, and have two independent driving motors in the system.

A Segway can be modeled as a two-wheeled inverted pendulum [16]. And its dynamics is governed by following equations. (Fig. 3.3) [17]:

$$\dot{\mathbf{x}} = \mathbf{Ax} + \mathbf{Bu} \quad (3.1)$$

$$\mathbf{y} = \mathbf{Cx} + \mathbf{Du} \quad (3.2)$$

where,

$$\mathbf{x} = \begin{bmatrix} x & \dot{x} & \psi & \dot{\psi} & \phi & \dot{\phi} \end{bmatrix}^T \quad (3.3)$$

$$\mathbf{u} = \begin{bmatrix} M_1 & M_2 \end{bmatrix}^T \quad (3.4)$$

where, M_1 and M_2 are the motor torques of the left and right wheels, and

$$\mathbf{A} = \begin{bmatrix} 0 & 1 & 0 & 0 & 0 & 0 \\ 0 & 0 & 0 & 0 & \frac{m_s^2 d_h^2 g}{3m_c I_y + 3m_c m_s d_h^2 + m_s I_y} & 0 \\ 0 & 0 & 0 & 1 & 0 & 0 \\ 0 & 0 & 0 & 0 & 0 & 0 \\ 0 & 0 & 0 & 0 & 0 & 1 \\ 0 & 0 & 0 & 0 & \frac{m_s d_h g (3m_c + m_s)}{3m_c I_y + 3m_c m_s d_h^2 + m_s I_y} & 0 \end{bmatrix} \quad (3.5)$$

$$\mathbf{B} = \begin{bmatrix} 0 & 0 \\ \frac{-(m_s d_h^2 + I_y)/R - m_s d_h}{3m_c I_y + 3m_c m_s d_h^2 + m_s I_y} & \frac{-(m_s d_h^2 + I_y)/R - m_s d_h}{3m_c I_y + 3m_c m_s d_h^2 + m_s I_y} \\ 0 & 0 \\ \frac{d/R}{6m_c (d/2)^2 + m_c R^2 + 2I_z} & \frac{-d/R}{6m_c (d/2)^2 + m_c R^2 + 2I_z} \\ 0 & 0 \\ \frac{-m_s d_h/R - 3m_c m_s}{3m_c I_y + 3m_c m_s d_h^2 + m_s I_y} & \frac{-m_s d_h/R - 3m_c m_s}{3m_c I_y + 3m_c m_s d_h^2 + m_s I_y} \end{bmatrix} \quad (3.6)$$



Figure 3.2: A Segway (©2011 Segway Inc.)

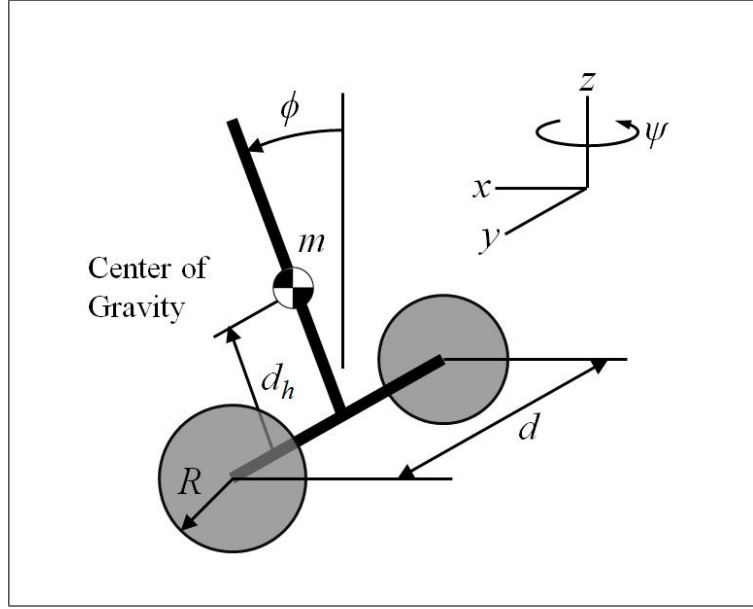


Figure 3.3: Coordinate system and kinematic assumptions

$$\mathbf{C} = \mathbf{I} \quad (3.7)$$

$$\mathbf{D} = \mathbf{0} \quad (3.8)$$

Table 3.2: *Major Mechanical Parameters

Parameters	Meanings	Values	Units
d_h	Distance from C.G. to Wheel Axis	0.1	m
m_s	Mass of the Body	17.8	kg
m_c	Mass of a Wheel	0.350	kg
I_y	y-directional Moment of Inertia	0.534	kgm^2

*Calculated according to the assumptions.

Some major mechanical parameters used in the governing equations are indicated in Table 3.2. One thing interesting here is that the six-dimensional system is controlled by only two control inputs, which is called a non-holonomic system — a system that has more outputs than inputs.

The dynamics introduced here is evaluated in the following section.

3.2.2 Three-Wheeled Vehicle and its Dynamics

Huston, Graves and Johnson first studied three-wheeled vehicle dynamics in 1982 [18]. They made stability comparisons between a three-wheeled vehicle with two wheels on the front axle (2F1R), a three-wheeled vehicle with two wheels on the rear axle (1F2R) and a standard four-wheeled vehicle, and concluded that three-wheeled vehicles can offer safe alternatives to four-wheeled vehicles.

In this subsection, two dynamic models which Huston et al. proposed are introduced and some modifications are made for EVs: it is assumed that two independent driving motors are equipped in the two front or rear wheels and the steering wheel(s) are in the front in both cases.

Three-Wheeled Vehicle (2F1R) and its Dynamics

The schematic of the system is shown in Fig. 3.4. Two independent driving motors are attached in the front steering wheels, and a non-driving-nor-steering wheel is in the rear.

$$\dot{\mathbf{x}} = \mathbf{Ax} + \mathbf{Bu} \quad (3.9)$$

$$\mathbf{y} = \mathbf{Cx} + \mathbf{Du} \quad (3.10)$$

where,

$$\mathbf{x} = \begin{bmatrix} \beta & \gamma \end{bmatrix}^T \quad (3.11)$$

$$\mathbf{u} = \begin{bmatrix} \delta & M_z \end{bmatrix}^T \quad (3.12)$$

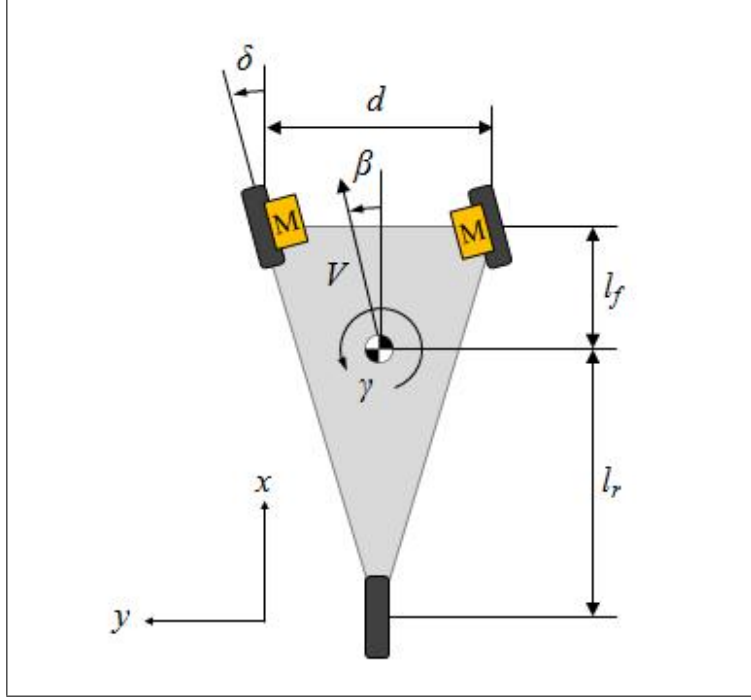


Figure 3.4: Three-wheeled vehicle model with two wheels on front axle.

and

$$\mathbf{A} = \begin{bmatrix} -\frac{2C_f + C_r}{mV} & -\frac{2l_f C_f - l_r C_r}{mV^2} \\ -\frac{2l_f C_f - l_r C_r}{I_z} & -\frac{2l_f^2 C_f + l_r^2 C_r}{I_z V} \end{bmatrix} \quad (3.13)$$

$$\mathbf{B} = \begin{bmatrix} \frac{2C_f}{mV} & 0 \\ \frac{2l_f C_f}{I_z} & \frac{1}{I_z} \end{bmatrix} \quad (3.14)$$

$$\mathbf{C} = \mathbf{I} \quad (3.15)$$

$$\mathbf{D} = \mathbf{0} \quad (3.16)$$

where, M_z is the direct yaw moment input, which is generated by independent driving motors of the front wheels.

Three-Wheeled Vehicle (1F2R) and its Dynamics

The schematic of the system is shown in Fig. 3.5. Two independent driving motors are attached in the rear wheels, and a non-driving steering wheel is in the front.

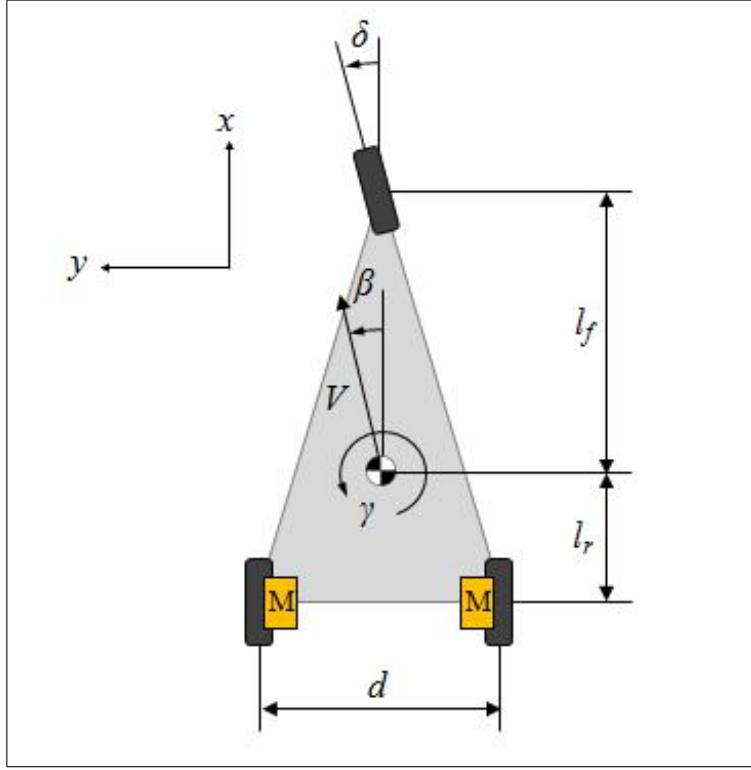


Figure 3.5: Three-wheeled vehicle model with two wheels on rear axle.

$$\dot{\mathbf{x}} = \mathbf{A}\mathbf{x} + \mathbf{B}\mathbf{u} \quad (3.17)$$

$$\mathbf{y} = \mathbf{C}\mathbf{x} + \mathbf{D}\mathbf{u} \quad (3.18)$$

where,

$$\mathbf{x} = \begin{bmatrix} \beta & \gamma \end{bmatrix}^T \quad (3.19)$$

$$\mathbf{u} = \begin{bmatrix} \delta & M_z \end{bmatrix}^T \quad (3.20)$$

and

$$\mathbf{A} = \begin{bmatrix} -\frac{C_f+2C_r}{mV} & -\frac{l_f C_f-2l_r C_r}{mV^2} \\ -\frac{l_f C_f-2l_r C_r}{I_z} & -\frac{l_f^2 C_f+2l_r^2 C_r}{I_z V} \end{bmatrix} \quad (3.21)$$

$$\mathbf{B} = \begin{bmatrix} \frac{C_f}{mV} & 0 \\ \frac{l_f C_f}{I_z} & \frac{1}{I_z} \end{bmatrix} \quad (3.22)$$

$$\mathbf{C} = \mathbf{I} \quad (3.23)$$

$$\mathbf{D} = \mathbf{0} \quad (3.24)$$

where, M_z is the direct yaw moment input, which is generated by independent driving motors of the rear wheels.

3.2.3 Four-Wheeled Vehicle and its Dynamics

Although the dynamic analyses for four-wheeled ground vehicles are plentiful, most of them are concerning the conventional engine-driven vehicles. In this section, a dynamic model for an independent motor driven electric vehicle, which is relatively rare, is introduced. The model is based on an electric vehicle called COMS3 of our research group (Figure 3.6), which is a modified Toyota Autobody's COMS for research purposes. (Note: parameters from Table 3.1 are used.)

For four-wheeled independent motor-driven electric vehicles, the governing equations are as below:

$$\dot{\mathbf{x}} = \mathbf{Ax} + \mathbf{Bu} \quad (3.25)$$

$$\mathbf{y} = \mathbf{Cx} + \mathbf{Du} \quad (3.26)$$

where,

$$\mathbf{x} = \begin{bmatrix} \beta & \gamma \end{bmatrix}^T \quad (3.27)$$

$$\mathbf{u} = \begin{bmatrix} \delta & M_z \end{bmatrix}^T \quad (3.28)$$

and

$$\mathbf{A} = \begin{bmatrix} -\frac{2(C_f+C_r)}{mV} & -\frac{2(l_f C_f - l_r C_r)}{mV^2} \\ -\frac{2(l_f C_f - l_r C_r)}{I_z} & -\frac{2(l_f^2 C_f + l_r^2 C_r)}{I_z V} \end{bmatrix} \quad (3.29)$$

$$\mathbf{B} = \begin{bmatrix} \frac{2C_f}{mV} & 0 \\ \frac{2l_f C_f}{I_z} & \frac{1}{I_z} \end{bmatrix} \quad (3.30)$$

$$\mathbf{C} = \mathbf{I} \quad (3.31)$$

$$\mathbf{D} = \mathbf{0} \quad (3.32)$$

where, M_z is the direct yaw moment input, which is generated by independent driving motors of the rear wheels.

3.3 Structural Stability Evaluation

Before starting the discussion on the EV compatibility of the systems above, it is necessary to consider safety issues, which naturally leads us to the structural stability problem.

Many automobile manufacturers and automotive component makers have been developing Electronic Stability Programs (ESP) for vehicle safety. They are mainly focusing on improving roll, yaw, and pitch stability utilizing electronically controlled engine and brake



Figure 3.6: IWM-driven EV COMS of Hori Laboratory: COMS3, COMS1, and COMS2 from the left.

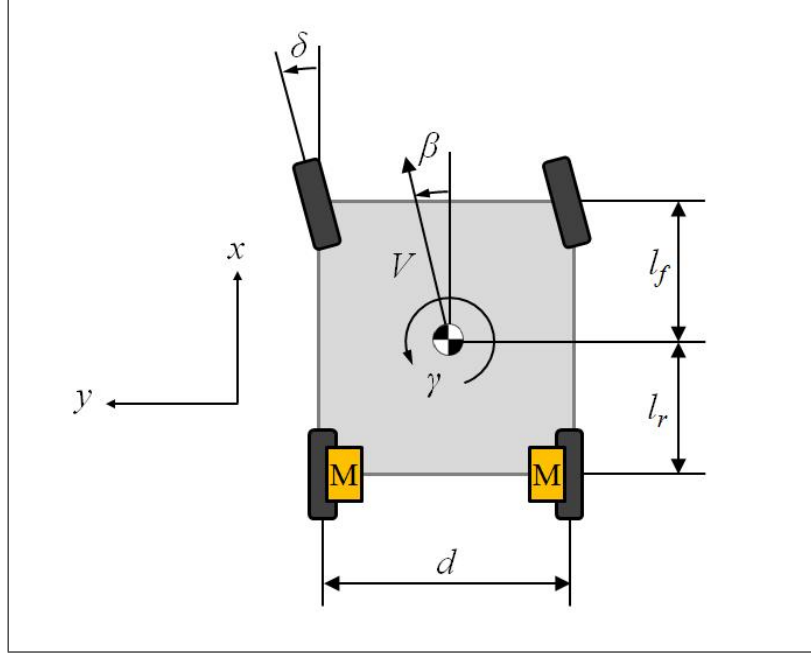


Figure 3.7: Planar model for the four-wheeled IWM-driven EV

systems, due to the fact that stabilizing those three is generally regarded crucial for vehicle safety.

Among those three, the roll stability control logic always has priority over the other two in any kind of ESP system. Rollover accidents have resulted in more than 9,000 fatalities and 200,000 non-fatal injuries in the United States annually, with a fatality rate second only to frontal collisions [19]. There is no difference in terms of safety even if the powertrain changes from ICE to IWM; in this thesis roll stability is checked in each of models introduced above.

Previous research works have introduced numerous criteria to quantify rollover stability [20], such as Static Stability Factor (SSF) [21], Load Transfer Metric (LTM) [22], Energy Stability Margin (ESM) [23], and Force-Angle Stability Metric (FAS) [25]. By applying each of these criteria to the models introduced in the previous section, the structural stability is checked.

3.3.1 Static Stability Factor (SSF)

Static Stability Factor is defined as the ratio of the lateral position of the vehicle center-of-gravity to the vertical position (Figure 3.8, Eq. 3.33) [21]. This criterion, however, is originally for the four-wheeled vehicle model. For two-wheeled and the three-wheeled models, the criterion is modified according to the shape of the base of support (Figure 3.9).

$$\text{SSF} = \frac{d}{2h} \quad (3.33)$$

where, larger values of SSF indicate greater stability.

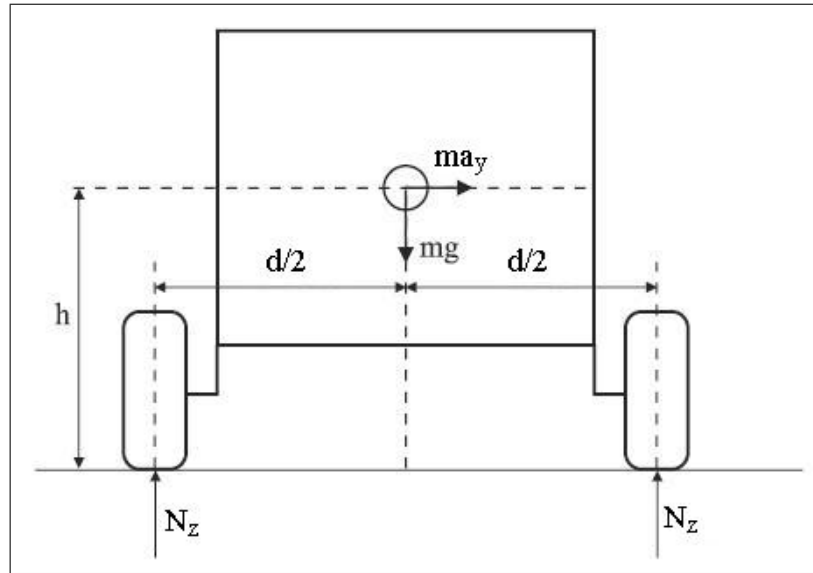


Figure 3.8: Static Stability Factor diagram [20]

Using the assumptions 1~4 made at the beginning of this chapter, a comparison is made with regard to SSF criterion. For 3-wheeled models, by the way, the fraction, which is perpendicular to the tip-over line, of the lateral acceleration a_y needs to be considered.

The SSF comparison result in Table 3.3 shows two-wheeled and four-wheeled vehicles are more stable than three-wheeled ones; note that two-wheeled vehicles have zero SSF in y-directional rotation (pitch).

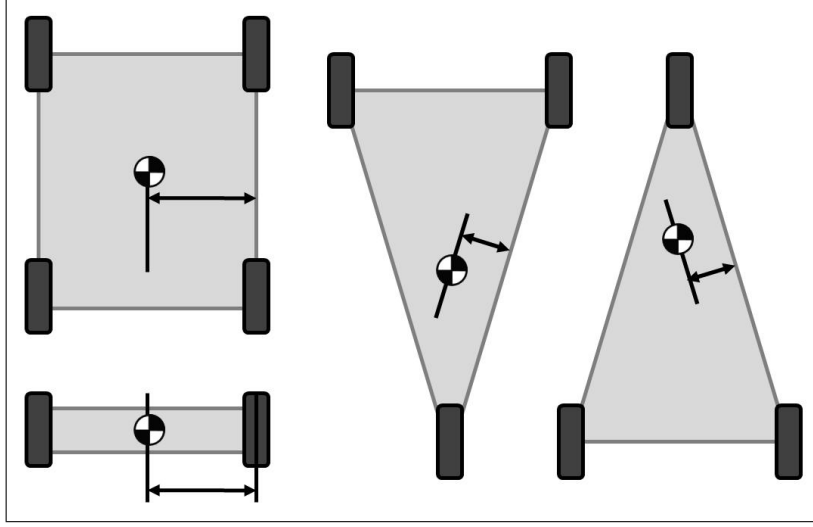


Figure 3.9: $d/2$ according to the shape of the base of support.

Table 3.3: SSF Roll Stability Comparison

2-Wheeled	3-Wheeled (2F1R)	3-Wheeled (1F2R)	4-Wheeled
1.11	0.74	0.74	1.11

3.3.2 Load Transfer Metric (LTM)

Load Transfer Metric estimates the difference in tire normal forces acting on each side of the vehicle so that it can indicate the nearness to wheel lift-off on smooth terrain. From the equilibrium of vertical forces and balance of roll moments, the rollover coefficient R is defined as [22]:

$$\mathbf{R} = \frac{N_{zR} - N_{zL}}{N_{zR} + N_{zL}} \simeq \frac{2ha_y}{dg} \quad (3.34)$$

Using the assumptions 1~4 made at the beginning of this chapter and the variation of d from Figure 3.9, a comparison is made as shown in Table 3.4.

In equation (3.34), if $N_{zR} = 0$ ($N_{zL} = 0$) then the right(left) wheel(s) lift off and the rollover coefficient takes on the value $R = -1$ ($R = 1$). Consequently the lateral acceleration a_y is limited to the lift-off point. The maximum lateral acceleration is the value when the

Table 3.4: Maximum Lateral Acceleration a_y by LTM [m/s^2]

2-Wheeled	3-Wheeled (2F1R)	3-Wheeled (1F2R)	4-Wheeled
10.89	7.26	7.26	10.89

wheel lift-off occurs. According to the result it can be said that the 2-wheeled and 4-wheeled vehicles are more structurally stable than the other two in terms of LTM.

3.3.3 Energy Stability Margin (ESM)

This metric was developed describing the minimum difference in potential energy between a given vehicle state and the vehicle state at rollover. In the literature [23] and [24], the Rollover Prevention Energy Reserve (RPER) function is defined as the difference between the energy terms V_{crit} and T_K at each instant in time t , where V_{crit} is the gravitational potential energy difference in between the current position and the rollover position, and T_K the kinetic energy capable of being transferred into gravitational potential energy. According to this definition, RPER can be expressed as

$$\mathbf{RPER} = V_{crit} - T_K \quad (3.35)$$

$$\mathbf{V}_{crit} = mgR_{AC}(1 - \sin \phi_0) \quad (3.36)$$

$$\mathbf{T}_K = \frac{1}{2}I_x\omega_t^2 \quad (3.37)$$

where, R_{AC} is the distance from the vehicle center of gravity to the rollover axis, ϕ_0 is the angle between R_{AC} and the horizontal plane, and ω_t is the component of vehicle angular velocity in the direction of rollover axis (Figure 3.10).

Assuming that the rollover axis is the line connecting right front wheel to right rear wheel, a comparison is made using ESM criterion.

The vehicle is easy to rollover when $RPER$ goes below zero. The values in Table 3.5 are calculated by putting $RPER = 0$. According to the result it can be said that the

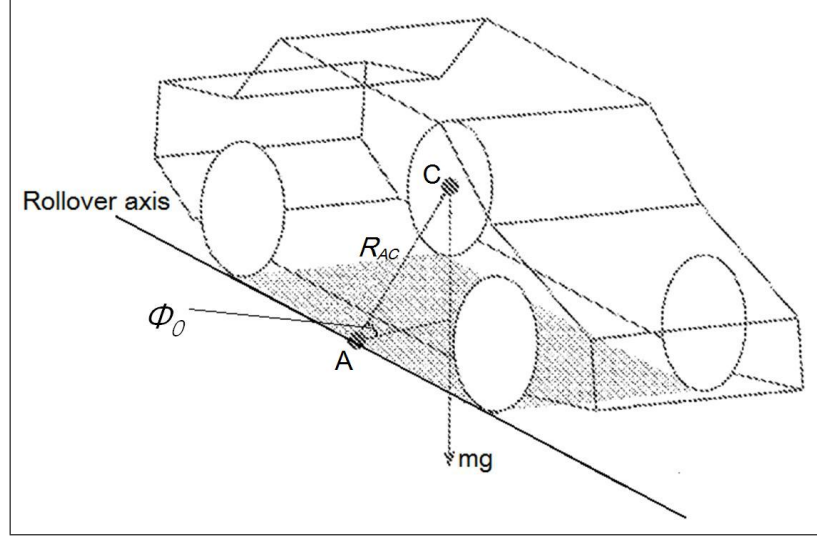


Figure 3.10: Gravitational Potential Energy Calculation (ESM) [24]

Table 3.5: Critical Angular Velocity ω_t by ESM [rad/sec]

2-Wheeled	3-Wheeled (2F1R)	3-Wheeled (1F2R)	4-Wheeled
18.63	16.78	16.78	18.63

2-wheeled and 4-wheeled vehicles are more structurally stable than the other two in terms of ESM criterion.

3.3.4 Force-Angle Stability Metric (FAS)

This metric is generally considered the state-of-the-art in stability measurement due to its flexibility and theoretical accuracy. In this approach, the vehicle's wheel-road contact point vectors p_i ($i = 1, 2, 3, \dots, n$) are defined, and the line vectors joining the neighboring two contact points are referred to as tip over axes, denoted r_i . (Figure 3.11)

$$\mathbf{r}_i = \mathbf{p}_{i+1} - \mathbf{p}_i \quad (3.38)$$

$$\mathbf{r}_n = \mathbf{p}_1 - \mathbf{p}_n \quad (3.39)$$

The moments SM_i caused by body forces and d'Alembert's force with respect to each

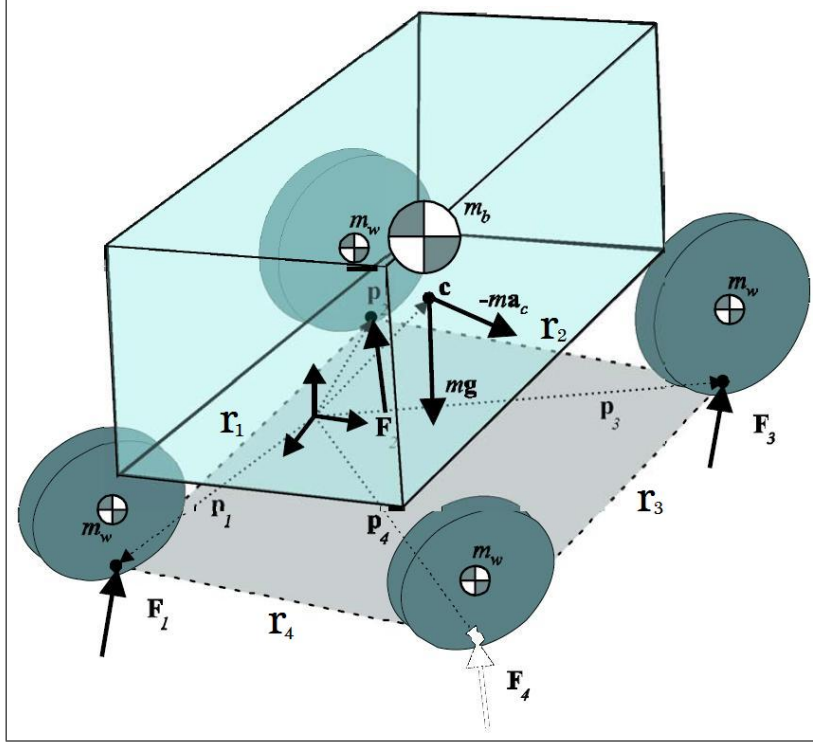


Figure 3.11: Free-body diagram for FAS [20]

tip over axis, as:

$$SM_i = \sum_{j=1}^k ((q_j - p_i) \times B_j) \cdot r_i - ((c - p_i) \times ma_c) \cdot r_i \quad (3.40)$$

where, B_j ($j = 1, \dots, k$) are k non-supporting body forces, and q_j are the corresponding acting points.

These moments can be normalized by the minimum static moment on flat ground, denoted SM_0 . The metric is then chosen as the minimum moment over all tip over axes:

$$\alpha = \min_i \left(\frac{SM_i}{SM_0} \right) \quad (3.41)$$

Substituting parameters indicated in Table 3.1, a comparison is made as shown in Table 3.6. SM_1 around the weakest axis r_1 , is checked in all cases, where $i = 1$ on the (right)

front wheel. Two-wheeled model is not evaluated because it has only one tip over axis, which is always controlled.

Table 3.6: FAS Roll Stability Comparison around Axis r_1 .

Case	α (Normalized SM)
2-Wheeled	—
3-Wheeled (2F1R)	$\alpha = 1 - 0.06a_x - 0.14a_y + 0.10a_z$
3-Wheeled (1F2R)	$\alpha = 1 + 0.06a_x - 0.14a_y + 0.10a_z$
4-Wheeled	$\alpha = 1 - 0.09a_y + 0.10a_z$

The vehicle is easy to rollover when α goes below zero. As observed in Table 3.6, all three models evaluated are equally affected by the vertical acceleration a_z , while the three-wheeled models are more easily affected by lateral acceleration a_y than the four-wheeled one. Moreover, the three-wheeled models are also affected by the longitudinal acceleration a_x . Note that the one with two front wheels is more easier to rollover when the vehicle is accelerating (positive a_x), while the other is more easier to rollover when braking (negative a_x).

In case we do the calculation for every tip-over axis of the vehicle, the result can be seen in Fig. 3.12. The color represents the value of the normalized SM , α . The horizontal and the vertical axes show the lateral a_y and longitudinal acceleration a_x in m/s^2 , respectively, when the vertical acceleration a_z is set zero. The dark area indicates where the normalized SM , α has a value below zero, i.e. the vehicle is easy to tip over. It can be seen that the 4-wheeled vehicle shows better FAS stability than the two 3-wheeled vehicles, while the 3-wheeled vehicles have higher mountain peaks than the 4-wheeled one in longitudinal directions.

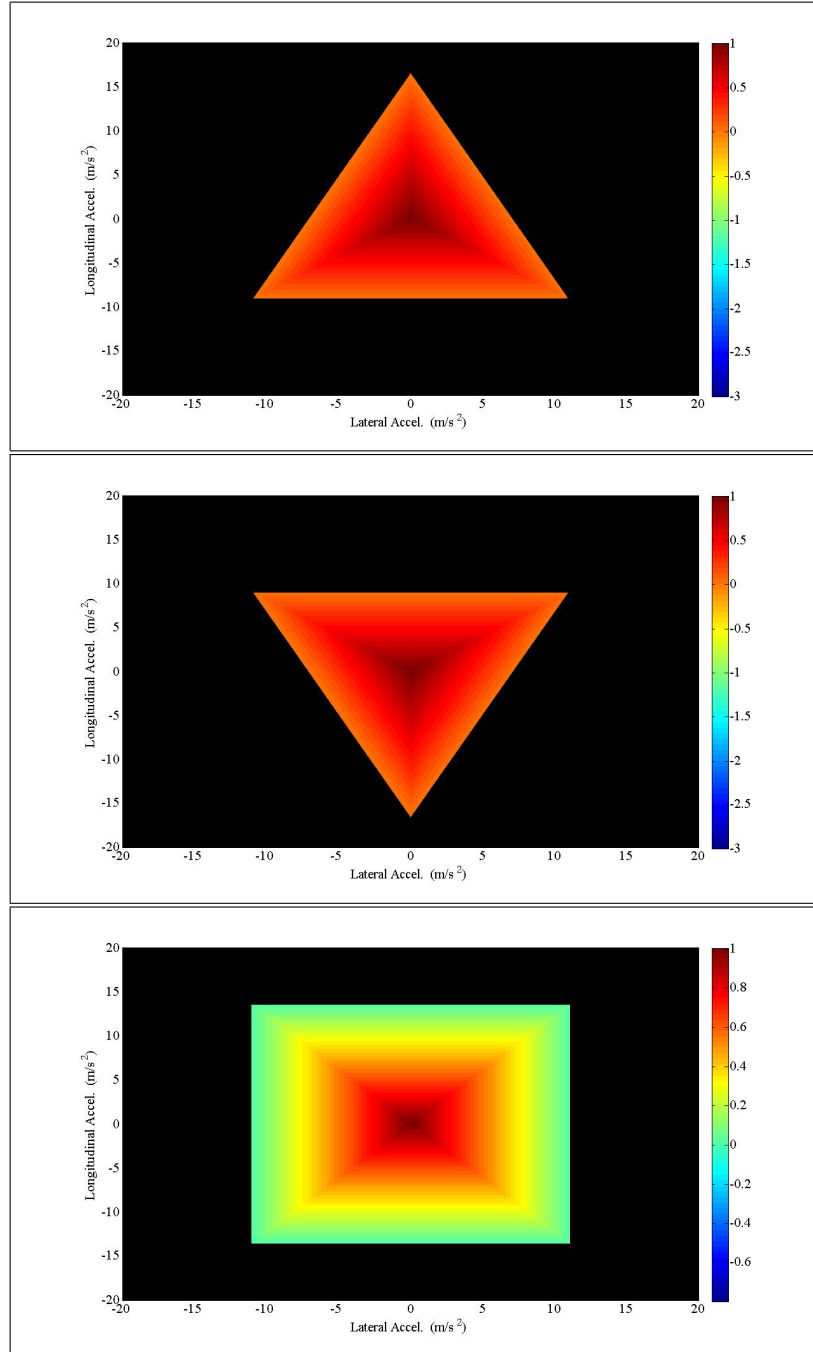


Figure 3.12: FAS plot for 2F1R(upper), 1F2R(middle), and 4W(lower) with respect to every roll-over axis.

3.4 Study on Compatibility with EV Motion Control

In this section, in order to see the compatibility of the system with EV motion control, the controllability and the system response of the vehicle dynamic models are evaluated. Firstly, the controllability of each system is observed. Secondly, the yaw rate responses are shown with respect to the steering input and the yaw moment input respectively, since we are dealing with two major inputs which distinguish EVs from the conventional engine vehicles from the motion control point of view. The mechanical parameters assumed in Table 3.1 are used in the evaluations.

3.4.1 Controllability

First of all, using the state equations (3.1)~(3.32) introduced in Section 3.2, the controllability of each system is checked. Controllability of a system can be clarified by calculating the rank of the matrix $\Gamma_c[A, B]$ which is defined by:

$$\Gamma_c[A, B] = \begin{bmatrix} B & AB & A^2B & \dots & A^{n-1}B \end{bmatrix} \quad (3.42)$$

The system is controllable if and only if $\Gamma_c[A, B]$ has full rank. This criterion is binary, i.e. it only provides ‘YES-NO’ answers, and the answers for the given systems are shown in Table 3.7.

Table 3.7: Controllability Check

	2W	2F1R	1F2R	4W	Remarks
$\text{rank}(\Gamma_c[A, B])/\text{Dimension}$	6/6	2/2	2/2	2/2	All full rank.
Controllability	YES	YES	YES	YES	All controllable.

However, in order to compare the controllabilities of the different systems, a quantitative measure is needed. To meet this demand, here is used the quantification method introduced by Eising [27], which provides a standard to measure how far a controllable system is

from an uncontrollable one. The distance $\mu(A, B)$ between a controllable system from an uncontrollable one is defined as follows:

$$\mu(A, B) \equiv \min \sigma_n(sI - A, B) \quad (3.43)$$

where $\sigma_n(sI - A, B)$ is the smallest singular value of $[sI - A, B]$. This criterion indicates the spacial distance from a system to its nearest uncontrollable point, which means when $\mu(A, B) = 0$ the system becomes uncontrollable if there is any parameter deviation in the system. According to the definition, the distances for the given systems are shown in Fig. 3.13.

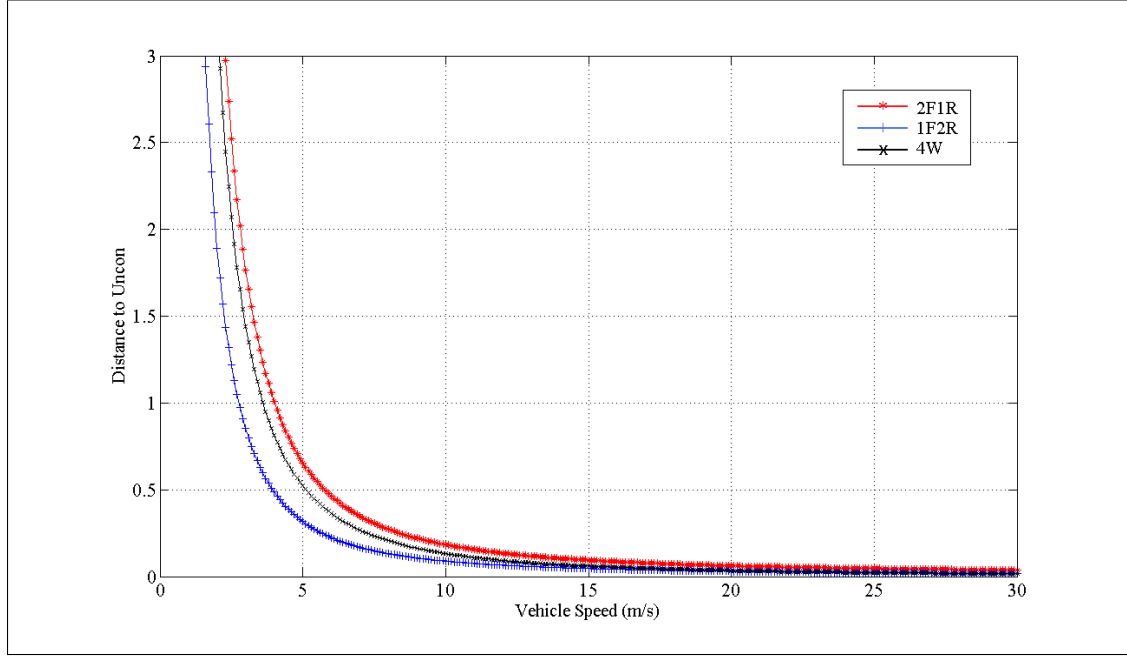


Figure 3.13: Distance to the Uncontrollability

The result shows that the relative controllability of the 3-wheeled vehicle which has two wheels on the front, is higher than that of the 4-wheeled vehicle at any vehicle speed, which implies that the 3-wheeled vehicles have better robustness against the parameter variation than the 4-wheeled ones. For applying this criterion, the system matrices need to be the same in dimension, thus two wheel model is not evaluated here.

3.4.2 Steering Input and Vehicle Yaw Response

For the vehicle yaw response analyses, state equations (3.1)~(3.32) are converted into transfer functions $G(s)$ as:

$$G(s) = C(sI - A)^{-1}B + D \quad (3.44)$$

Figure 3.14 shows the responses of the vehicle models in time domain when there is given a step steering input whose magnitude is 30 degrees which is usually the maximum value for passenger vehicles at $t = 0$. It can be seen that the 3-wheeled vehicle models are slower in response than the 4-wheeled one, however, the difference is not so big; the vehicle speed is dominant, not the chassis structure. The 2-wheeled vehicle is excluded because it does not have the steering input.

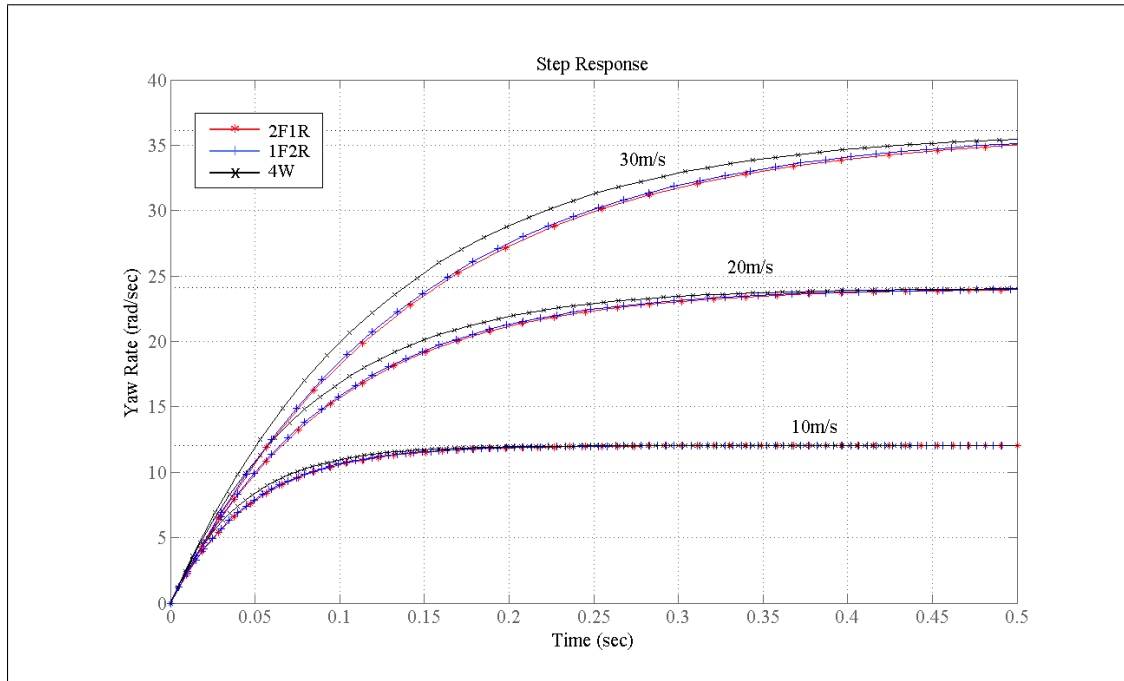


Figure 3.14: Step Steering Input (30 degrees) vs. Vehicle Yaw Response

Moreover, as it can be seen in Fig. 3.15 the frequency response to the steering input is dependent on the vehicle speed; the wheel placement is not dominant.

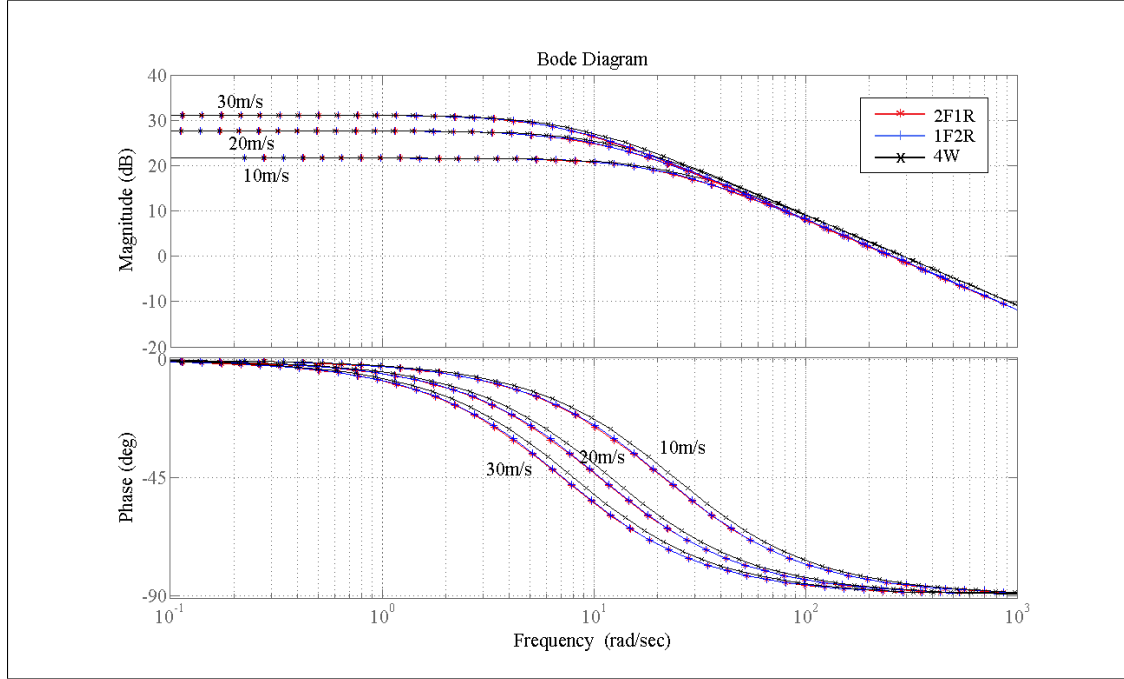


Figure 3.15: Bode Plot: Steering Input vs. Vehicle Yaw Response

3.4.3 Direct Yaw Moment Input and Vehicle Yaw Response

When there exists the difference between traction forces generated by two driving wheels, yaw moment occurs to the vehicle, which distinguishes EVs from the conventional engine vehicles. This difference is regarded as another input variable: the direct yaw moment input.

Using (3.44), the transfer functions are calculated for the analyses. Fig. 3.16 shows the yaw responses of the vehicles in time domain when there is given a step yaw moment input whose magnitude is of 80% of the vertical load of each case, which is usually the maximum friction on a dry asphalt, at $t = 0$. It can be seen that the response speed of the 3-wheeled vehicles is faster than that of the 4-wheeled one. Moreover, the steady state gain of the 3-wheeled vehicles is remarkably bigger than that of the 4-wheeled one at any longitudinal speed. This difference in gain can be explained by taking a look into the transfer functions governing the dynamics.

$$G(0)_{\gamma M_z} = \begin{cases} \frac{V(2C_f+C_r)}{2L^2C_fC_r(1-\frac{m(2l_fC_f-l_rC_r)V^2}{2C_fC_rL^2})} = \frac{3V}{2L^2C_3} = \frac{3V}{8L^2C_0} & (2F1R) \\ \frac{V(C_f+2C_r)}{2L^2C_fC_r(1-\frac{m(l_fC_f-2l_rC_r)V^2}{2C_fC_rL^2})} = \frac{3V}{2L^2C_3} = \frac{3V}{8L^2C_0} & (1F2R) \\ \frac{V(2C_f+2C_r)}{4L^2C_fC_r(1-\frac{m(l_fC_f-l_rC_r)V^2}{2C_fC_rL^2})} = \frac{V}{L^2C_4} = \frac{V}{3L^2C_0} & (4W) \end{cases} \quad (3.45)$$

where C_3 and C_4 are the cornering stiffnesses for the 3-wheeled and 4-wheeled vehicles according to the definition in Table 3.1, respectively, and C_0 is an arbitrary coefficient. From this observation, it is obvious that the difference in gain results from the difference of the cornering stiffness, which is a mechanical stiffness hindering the direct yaw moment input from turning the vehicle.

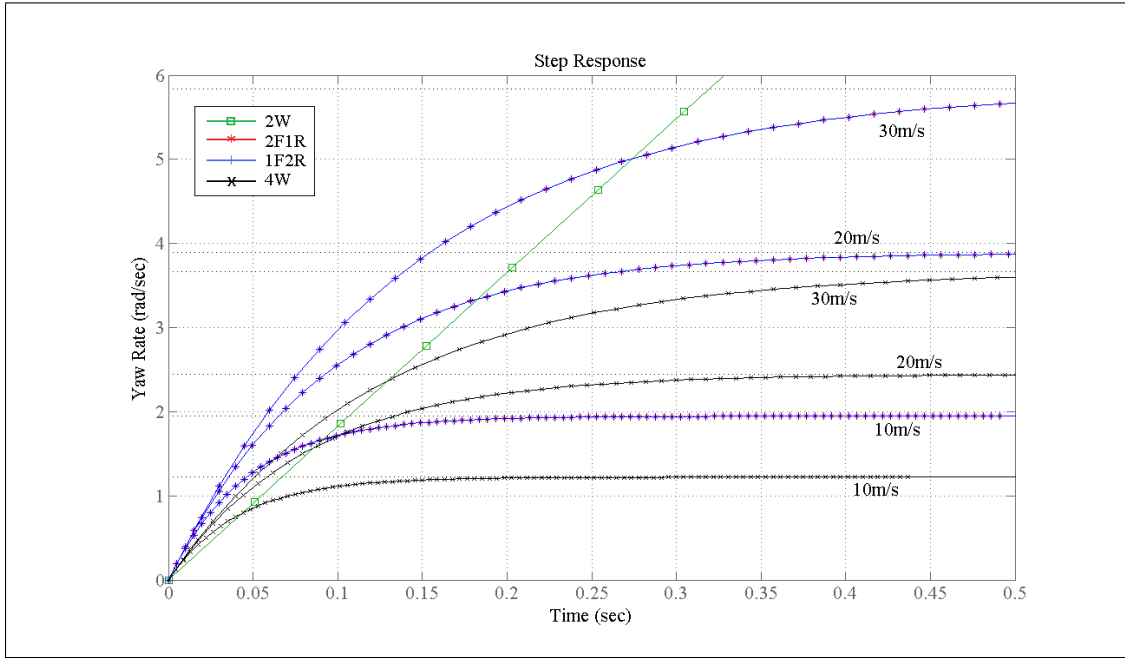


Figure 3.16: Step Direct Yaw Moment Input vs. Vehicle Yaw Response

Moreover, in Fig. 3.17 it can be seen that the frequency response is almost the same as Fig. 3.15, but only exists difference in gain. Such relatively small gain makes it difficult for

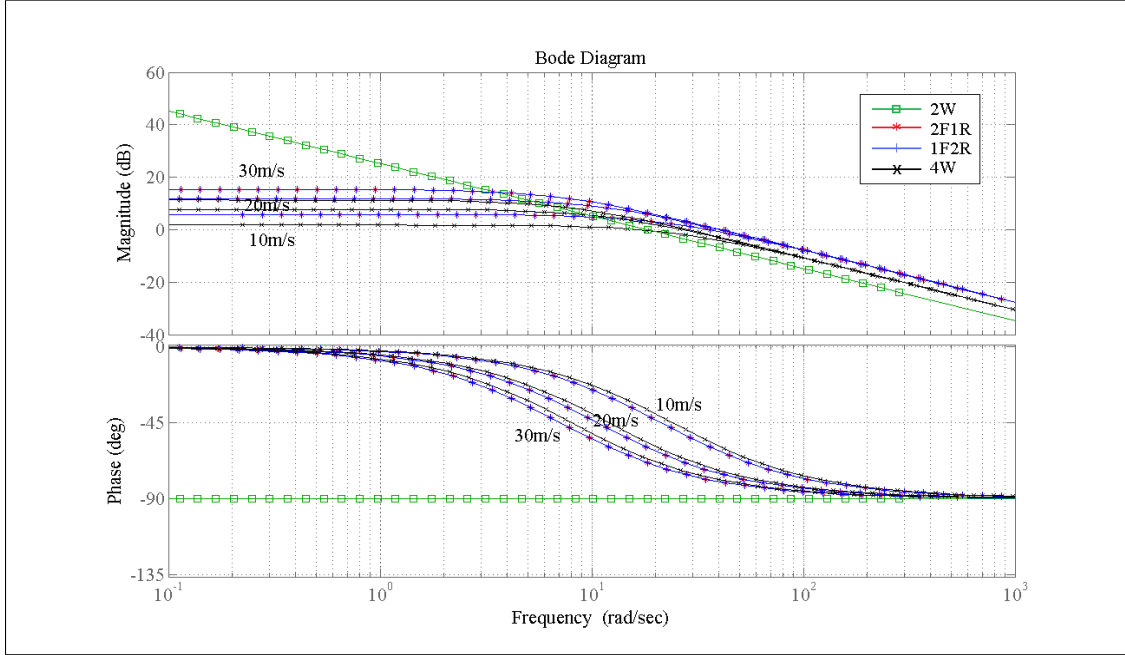


Figure 3.17: Bode Plot: Direct Yaw Moment Input vs. Vehicle Yaw Response

the direct yaw moment input to contribute in EV motion control. Here need improvements to be made to fully utilize ‘two inputs’ of the independent motor driven EVs.

Lastly, the behavior of the 2-wheeled vehicle is natural: the direct yaw moment gives the vehicle a constant angular acceleration — a linear increase in yaw rate, which can be seen in Fig. 3.16 and 3.17.

3.5 Summary

In this chapter, we made an observation on the vehicle structural stability using various criteria from the literature: SSF, LTM, ESM, and FAS, and checked the compatibility of the systems from the EV motion control point of view.

To summarize the results:

- Generally, the 4-wheeled vehicle is the most structurally stable by all criteria as shown in Table 3.8.

Table 3.8: Structural Stability Summary.

Criterion	2W	2F1R	1F2R	4W	Remarks
SSF	1.11	0.74	0.74	1.11	higher value indicates higher stability
LTM	10.89	7.26	7.26	10.89	maximum lateral acceleration [m/s^2]
ESM	18.63	16.78	16.78	18.63	x-directional maximum angular velocity [rad/s]
FAS	N/A	—	—	—	See Fig. 3.12

- All vehicle models are controllable. However, as seen in Fig. 3.13, in terms of robustness the 3-wheeled vehicle with two wheels on the front is the most farthest from the uncontrollability, even farther than the 4-wheeled one. (2-wheeled model is excluded.)
- In response to a unit step steering input, no big difference can be observed among those of all vehicle models. The response is mainly dominated by the vehicle longitudinal speed.
- In response to a unit step yaw moment input, all models seem almost the same in response speed. However, the 3-wheeled models show larger static gain than the 4-wheeled one. This can be explained in the observation made by (3.45): the mechanical stiffness makes the difference.
- In all cases, the gain of $G(s)_{\gamma\delta}$ is about 10 times larger than $G(s)_{\gamma M_z}$. The two inputs, which distinguish EVs from the conventional engine vehicles, have too large gap in between, where improvements need to be made.

From the observations made in this chapter, it is clear that: when trying to find a novel chassis structure for the independent motor driven EVs, there are some efforts need to be made: to reduce mechanical stiffness hindering the direct yaw moment input from turning the vehicle, and to maintain structural stability and controllability of the system.

Chapter 4

A Novel Chassis Structure for EVs using Caster Wheels and Independent Driving Motors

4.1 Introduction

Based on the observations and consequent conclusions made in the previous chapter, this thesis proposes a novel structure using caster wheels and independent driving motors, as one of the possible chassis configurations for the future passenger electric vehicles. The system consists of two independent driving wheels and two caster wheels. This configuration enables the vehicle to have: a low mechanical stiffness against the direct yaw moment input because caster wheels are free to rotate; and a high static stability because the vehicle has four wheels, which showed the highest static stability from the observation in the previous chapter.

Here in this chapter, an experimental vehicle CIMEV (Fig. 4.4), which is fabricated to verify the feasibility of the proposed chassis structure, is introduced. Considerations made during the design process are derived here. The dynamic behaviors of the system are shown with experimental data, and corresponding control strategies are discussed. The advantages of the proposed vehicle structure are shown along with comparisons made between the conventional vehicles. Finally possible applications of the proposed system are considered, including not only passenger vehicles, but many other industrial and military applications.

4.2 Caster Wheels and Vehicle Dynamics

A caster wheel is an undriven wheel that is free to move or rotate (Fig. 4.1). By choosing caster wheels as steering wheels, the effect of traction and braking force distribution generated by driving wheels on the vehicle dynamics can be maximized. In addition to this, the unique dynamic characteristics of caster wheel itself can affect the vehicle motion, which allows the vehicle to have expanded mobility.

Although caster wheels can be found in numerous applications, including shopping carts, chairs, mobile robots and even the aircraft landing gears, their dynamics has not been satisfactorily addressed yet with regard to the vehicle dynamics. For instance, it is sometimes neglected as in [29], being described as a point only exerting normal force from the ground to the vehicle body.

In order to fully utilize the advantages of using independent driving motors in vehicle powertrain-chassis system, the caster behavior needs to be examined being linked to vehicle dynamics. In literature, most of the studies regarding the caster wheel dynamics are provided by those who are making mobile robots or aircrafts. The latter are concerning about the vibration of an aircraft landing gear during taxiing, thus they are focusing on attenuating the phenomenon at high operation speed [30]. Meanwhile, the former are more



Figure 4.1: A caster wheel [28]

into the kinematics of the system, and more likely to neglect the transient dynamics. Caster wheels are not seen in vehicle dynamics for passenger vehicles so far.

However, among the dynamic models provided by the aforementioned research groups, the model suggested by G. Somieski [30] seems to be compatible for our system. The system is modeled neglecting the existence of steering motors, and it is assumed that the casters are free to rotate only under the effect of the stiffness K and the damping D about the king pin. The governing equations are written as:

$$I_w \ddot{\delta} + D \dot{\delta} + K \delta = -M_{sa}(\alpha) - e F_y(\alpha) - D_t(V) \dot{\delta} \quad (4.1)$$

$$\alpha = \delta - \theta_V \quad (4.2)$$

where

I_w : moment of inertia of the caster about the (z-directional) king pin;

D : damping constant about the king pin;

K : spring constant about the king pin;

M_{sa} : self aligning torque;

e : caster arm length;

F_y : lateral force at the tire-road interface;

D_t : damping moment due to tread width;

α : side slip angle of the wheels; and

θ_V : direction of the velocity at the wheel.

Considering the size and the type of the wheel we are dealing with, which is 0.1m in diameter (Table 3.1) and hard-rubber made, the terms $M_{sa}(\alpha)$ and $D_t(V) \dot{\delta}$ can be reasonably neglected. Moreover, since $F_y(\alpha)$ can be approximated into a linear form of $F_y(\alpha) = C_f \alpha$, we can rewrite (4.1) simply as [13][31][32][33]:

$$I_w \ddot{\delta} + D \dot{\delta} + K \delta = -e C_f \alpha \quad (4.3)$$

This caster dynamics interacts with the vehicle dynamics through the liaison moments transmitted through and about the king pin, defined as:

$$M_{lias} = (Ds + K) \delta \quad (4.4)$$

This moment can also be written in the equivalent form of cornering force Y_{corn} , whose direction is along the y -axis, as:

$$Y_{corn} = \frac{M_{lias}}{e} \cos \delta \simeq \frac{M_{lias}}{e} \quad (4.5)$$

Thus we can finally describe the dynamic behavior of the vehicle with caster wheels, by substituting equations (4.4) and (4.5) into (2.30)~(2.33). The descriptions are derived in the following section.

4.3 Experimental Vehicle and its Modeling

4.3.1 Consideration of Wheel Placement

There are two caster wheels and two non-steered driving wheels within the system, and how to arrange them is a good engineering question. Reasonably two different system configurations are thinkable: one with the casters on the front axle, and the other with the casters on the rear as shown in Fig. 4.2.

Equations for System (a)

From equations (2.30)~(2.33) and (4.1)~(4.5), and considering that geometrically θ_V can be approximated as:

$$\theta_V = \beta + \frac{l_f}{V} \gamma \quad (4.6)$$

for front wheels, and

$$\theta_V = \beta - \frac{l_r}{V} \gamma \quad (4.7)$$

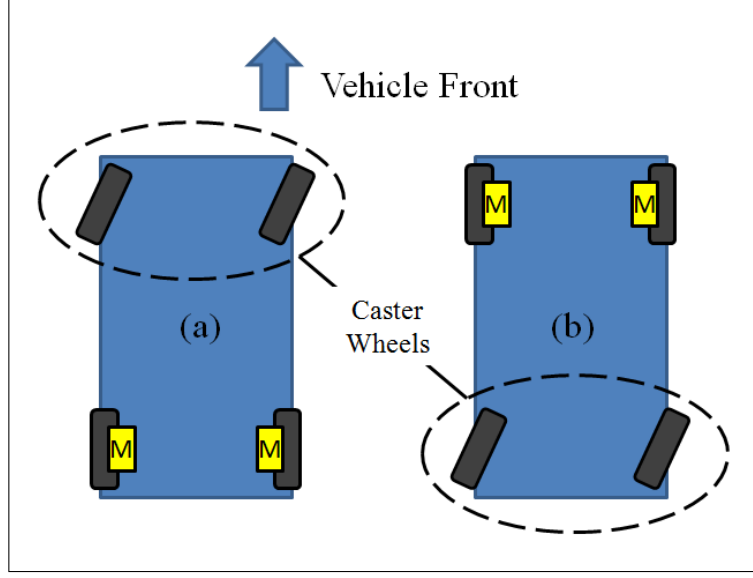


Figure 4.2: Two systems analyzed: System (a) has two driving motors on the rear axle, and two caster wheels on the front. Meanwhile, System (b) has two driving motors on the front axle, and two caster wheels on the rear.

for rear wheels, we can describe the system (a) as:

$$I_w \ddot{\delta}_F + D \dot{\delta}_F + (K + eC_f) \delta_F = eC_f \beta + \frac{el_f C_f}{V} \gamma \quad (4.8)$$

$$I_z \dot{\gamma} = \frac{l_f}{e} (2D \dot{\delta}_F + 2K \delta_F) - 2l_r C_r (\beta - \frac{l_r}{V} \gamma) + M_z \quad (4.9)$$

$$mV(\dot{\beta} + \gamma) = \frac{1}{e} (2D \dot{\delta}_F + 2K \delta_F) + 2C_r (\beta - \frac{l_r}{V} \gamma) \quad (4.10)$$

Equations (4.8)~(4.10) are converted into a state space model, by putting:

$$\mathbf{x}_F = \begin{bmatrix} \delta_F \\ \dot{\delta}_F \\ \beta \\ \gamma \end{bmatrix} \quad (4.11)$$

$$\dot{\mathbf{x}}_F = \mathbf{A}_F \mathbf{x}_F + \mathbf{B}_F \mathbf{M}_z \quad (4.12)$$

$$\mathbf{y}_F = \mathbf{C} \mathbf{x}_F \quad (4.13)$$

where

$$\mathbf{A}_F = \begin{bmatrix} 0 & 1 & 0 & 0 \\ -\frac{K+eC_f}{I_w} & -\frac{D}{I_w} & \frac{eC_f}{I_w} & \frac{el_fC_f}{I_wV} \\ \frac{2K}{emV} & \frac{2D}{emV} & \frac{2C_r}{mV} & -\frac{2l_rC_r}{mV^2} - 1 \\ \frac{2l_fK}{eI_z} & \frac{2l_fD}{eI_z} & -\frac{2l_rC_r}{I_z} & \frac{2l_r^2C_r}{I_zV} \end{bmatrix} \quad (4.14)$$

$$\mathbf{B}_F = \begin{bmatrix} 0 \\ 0 \\ 0 \\ \frac{1}{I_z} \end{bmatrix} \quad (4.15)$$

$$\mathbf{C}_F = \mathbf{I} \quad (4.16)$$

Equations for System (b)

In the same way,

$$I_w\ddot{\delta}_R + D\dot{\delta}_R + (K + eC_r)\delta_R = eC_r\beta - \frac{el_rC_r}{V}\gamma \quad (4.17)$$

$$I_z\dot{\gamma} = 2l_fC_f(\beta + \frac{l_f}{V}\gamma) - \frac{l_r}{e}(2D\dot{\delta}_R + 2K\delta_R) + M_z \quad (4.18)$$

$$mV(\dot{\beta} + \gamma) = \frac{1}{e}(2D\dot{\delta}_R + 2K\delta_R) + 2C_f(\beta + \frac{l_f}{V}\gamma) \quad (4.19)$$

Equations (4.17)~(4.19) are converted into a state space model, by putting:

$$\mathbf{x}_R = \begin{bmatrix} \delta_R \\ \dot{\delta}_R \\ \beta \\ \gamma \end{bmatrix} \quad (4.20)$$

$$\dot{\mathbf{x}}_R = \mathbf{A}_R\mathbf{x}_R + \mathbf{B}_R\mathbf{M}_z \quad (4.21)$$

$$\mathbf{y}_R = \mathbf{C}\mathbf{x}_R \quad (4.22)$$

where

$$\mathbf{A}_R = \begin{bmatrix} 0 & 1 & 0 & 0 \\ -\frac{K+eC_r}{I_w} & -\frac{D}{I_w} & \frac{eC_r}{I_w} & -\frac{el_rC_r}{I_wV} \\ \frac{2K}{emV} & \frac{2D}{emV} & \frac{2C_f}{mV} & \frac{2l_fC_f}{mV^2} - 1 \\ -\frac{2l_rK}{eI_z} & -\frac{2l_rD}{eI_z} & \frac{2l_fC_f}{I_z} & \frac{2l_f^2C_f}{I_zV} \end{bmatrix} \quad (4.23)$$

$$\mathbf{B}_R = \begin{bmatrix} 0 \\ 0 \\ 0 \\ \frac{1}{I_z} \end{bmatrix} \quad (4.24)$$

$$\mathbf{C}_R = \mathbf{I} \quad (4.25)$$

Comparison between System (a) and (b) in terms of Controllability

By using equations (4.8)~(4.25), the controllabilities of the two systems are analyzed. The rank of the matrix $\Gamma_c[A, B]$ of (3.7) is checked substituting parameters in Table 3.1. Both systems have dimension of 4, and the rank of $\Gamma_c[A, B]$ turns out to be 4 in both cases, i.e. there exist V , K , and D with which both the system (a) and (b) are completely controllable. As mentioned in the previous chapter, however, this criterion does not indicate how far the system is from the uncontrollability or how well the system is controllable. And it is difficult to find the combinations of V , K , and D which make the system uncontrollable.

In order to have further insight into the difference between the two systems, the method proposed by Eising [27] is used again. As shown in Fig. 4.3, relative controllability of the two systems is shown using equation (3.43). At a low vehicle speed around $1m/s$, both systems have high controllability with a small damping D . However, as vehicle speed increases, while the system (a) remains away from 0, the system (b) loses its controllability at a certain D . Overall distance to the uncontrollability is bigger in the system (a) than (b). Generally it can be said that the system (a) has higher controllability than (b) does, which implies that if there exists parameter variation in the system, the system (b) easily becomes uncontrollable than the system (a).

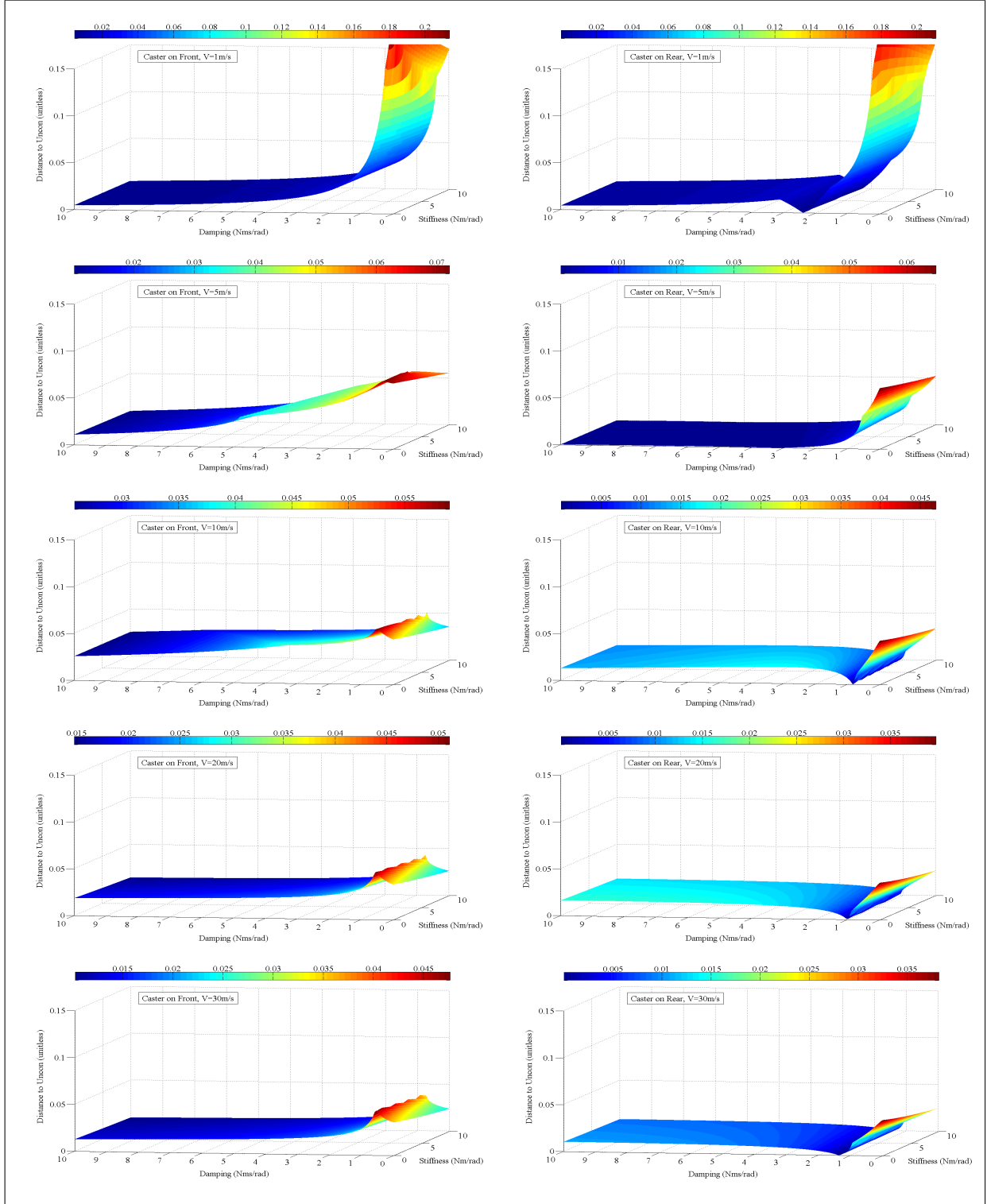


Figure 4.3: Distance to the uncontrollability, when spring K , and damping D are varying: system (a) on the left, and system (b) on the right; vehicle speed at 1, 5, 10, 20, 30 m/s from the top.

4.3.2 Experimental Vehicle, CIMEV

Based on the consideration made above, the experimental vehicle is designed to have two steering motors on the front, and two independent driving motors on the rear, in order to achieve higher controllability.

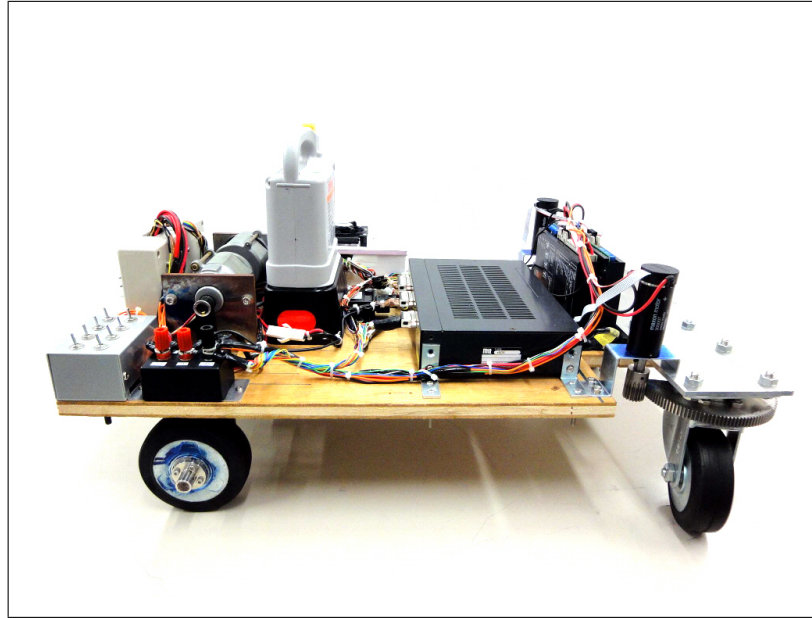


Figure 4.4: Caster wheeled electric vehicle CIMEV. Two rear wheels are driven via belt and pulley by two independent driving motors (90 Watts each). Two front wheels are casters, connected via gears to two independent steering motors (60 Watts each).

CIMEV (Caster-wheeled Independent Motor-driven Electric Vehicle, Fig.4.4) is designed to run unmanned. It is controlled by a digital signal processor (S-BOX) with two input signals transmitted through a radio controller. The PWM signals of the radio controller interpreted by the receiver are sent into the DSP, where they are linearized to drive the motors – both driving and steering – to run the vehicle. Four independently controlled electric motors are used in the system. Two are used for steering and the other two for driving. The vehicle is powered by a 24V Ni-MH battery. All power in need is supplied from this battery through DC/DC converters to adapt voltages. System configuration is

shown in Fig. 4.5. The arrangement of the sensors, actuators, and the power units can be seen.

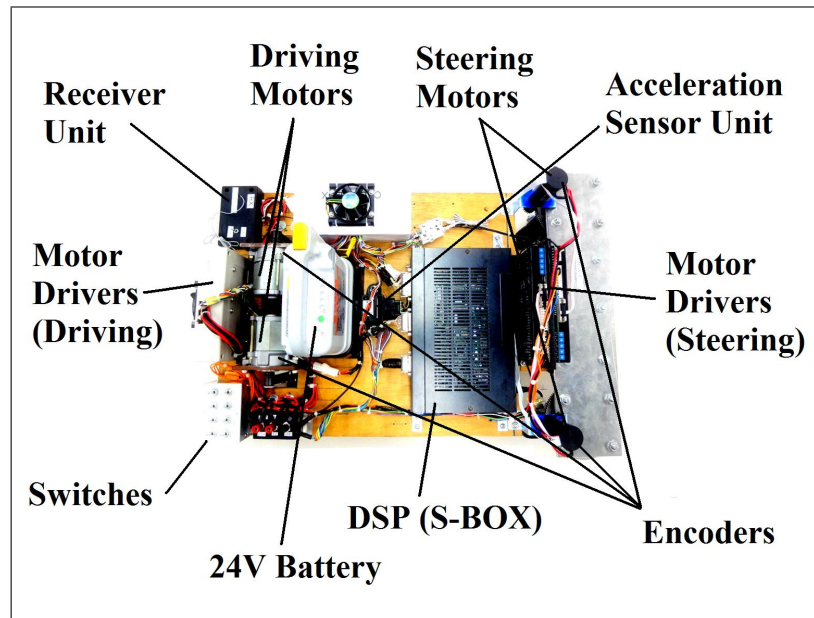


Figure 4.5: System configuration of the experimental vehicle CIMEV. The vehicle is controlled by a digital signal processor (S-BOX) with a remote controller. Its dynamic behavior is monitored and recorded through an acceleration sensor unit and four encoders.

Measured vehicle parameters are shown in Table 4.1, and the dimensions and the frame of reference are shown in Fig. 4.6. The specification of the driving and the steering motors are shown in Table 4.2 and Table 4.3, respectively. These motors are connected to the moving parts through timing belts and gears at certain reduction ratios. Additionally, the DSP (S-BOX) I/O setting is shown in Table 4.4. The sampling time of DSP is set $1ms$.

Four encoders are attached to each of motors to monitor the rotation of both the steering and the driving motors. Two encoders for the driving motors have the resolution of $3600pulse/rotation$, and the others for the steering motors are with the resolution of $1024pulse/rotation$. Additionally, an acceleration sensor unit (Fig. 4.7) is used to monitor the dynamic behavior of the vehicle.

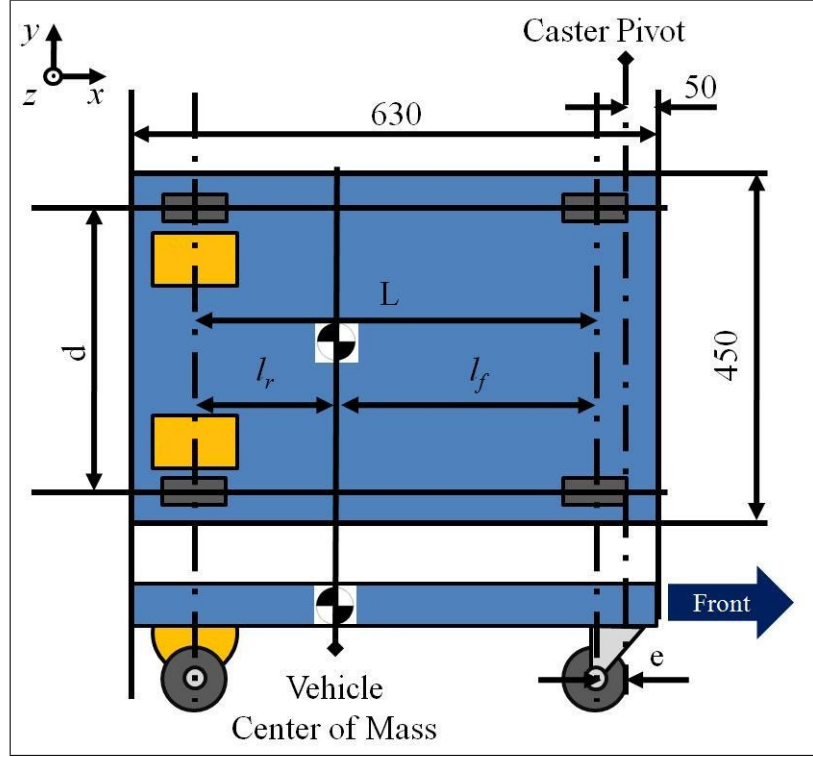


Figure 4.6: Vehicle dimensions and the frame reference.



Figure 4.7: Acceleration sensor unit used in the system. Yaw rate, x-directional, and y-directional accelerations can be measured.

4.3.3 Mathematical Modeling

As the experimental vehicle having been provided with two steering motors (Fig. 4.8), equations (4.8)~(4.10) need to be revised as below, considering the torque inputs of the

Table 4.1: Measured Vehicle Parameters

Parameters	Meanings	Values
m	Vehicle mass	18.5 <i>kg</i>
N_f	Normal force on each front wheel	39.2 <i>N</i>
N_r	Normal force on each rear wheel	51.5 <i>N</i>
I_z	Moment of inertia (vehicle)	0.409 <i>kgm</i> ²
I_w	Moment of inertia (caster wheel)	0.009 <i>kgm</i> ²
e	Caster arm length	0.040 <i>m</i>
l_f	Distance, from C.G. to front axle	0.247 <i>m</i>
l_r	Distance, from C.G. to rear axle	0.188 <i>m</i>
L	Wheel base	0.435 <i>m</i>
d	Tire track	0.355 <i>m</i>

Table 4.2: Specification of driving motor

Parameters	Meanings	Values
P_{rd}	Rated power	90 <i>W</i>
$K_{\tau d}$	Torque coefficient	0.093 <i>N · m/A</i>
K_{ed}	Back EMF coefficient	0.093 <i>V/(rad/s)</i>
R_{id}	Internal resistance	0.6 Ω
N_{nd}	Rotational speed without load	2350 <i>rpm</i>
I_{nd}	Current without load	0.6 <i>A</i>
J_{md}	Moment of inertia of roter	0.000071 <i>kgm</i> ²
r_{rd}	Reduction ratio (belt and pulley)	14 : 25

steering motors, and regarding that the liaison moments (Eq.(4.4)) and the equivalent forces (Eq.(4.5)) are given by the motors:

Table 4.3: Specification of steering motor

Parameters	Meanings	Values
P_{rs}	Rated power	60 W
$K_{\tau s}$	Torque coefficient	0.0538 N · m/A
K_{es}	Back EMF coefficient	0.0536 V/(rad/s)
R_{is}	Internal resistance	2.52 Ω
N_{ns}	Rotational speed without load	8490 rpm
I_{ns}	Current without load	0.0785 A
J_{ms}	Moment of inertia of rotor	0.00000345 kgm ²
r_{rs}	Reduction ratio (gears)	18 : 120

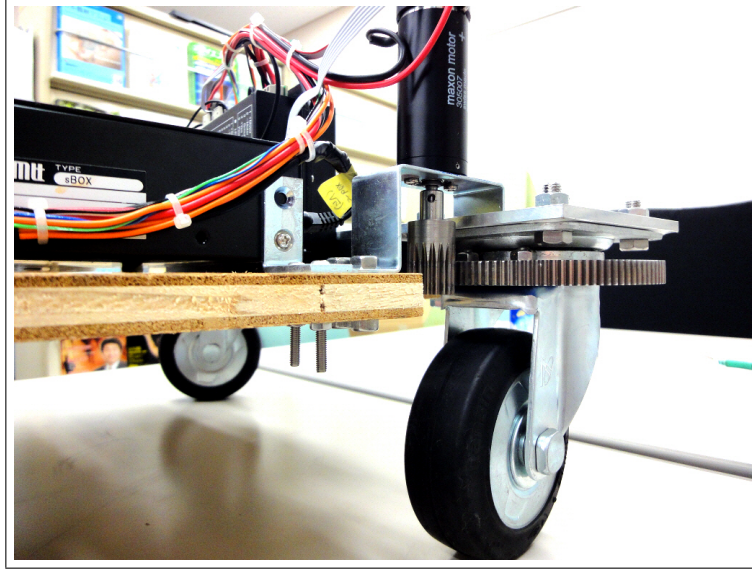


Figure 4.8: Caster wheel with steering motor.

$$I_w \ddot{\delta}_L + eC_f \delta_L = eC_f \beta + \frac{el_f C_f}{V} \gamma + T_{mL} \quad (4.26)$$

$$I_w \ddot{\delta}_R + eC_f \delta_R = eC_f \beta + \frac{el_f C_f}{V} \gamma + T_{mR} \quad (4.27)$$

$$I_z \dot{\gamma} = \frac{l_f}{e} (T_{mL} + T_{mR}) - 2l_r C_r (\beta - \frac{l_r}{V} \gamma) + M_z \quad (4.28)$$

$$mV(\dot{\beta} + \gamma) = \frac{1}{e} (T_{mL} + T_{mR}) + 2C_r (\beta - \frac{l_r}{V} \gamma) \quad (4.29)$$

Table 4.4: DSP(S-BOX) I/O Settings

Channel	Parameters	Meanings
<i>CNT1</i>	ω_L	Wheel Speed (L)
<i>CNT2</i>	ω_R	Wheel Speed (R)
<i>CNT3</i>	δ_L	Steering Angle (L)
<i>CNT4</i>	δ_R	Steering Angle (R)
<i>DI1</i>	—	Radio Controller CH1
<i>DI2</i>	—	Radio Controller CH2
<i>DI3</i>	—	Radio Controller CH3
<i>DI4</i>	—	Radio Controller CH4
<i>AD1</i>	T_L	Driving Motor Torque (L)
<i>AD2</i>	T_R	Driving Motor Torque (R)
<i>AD3</i>	T_{mL}	Steering Motor Torque (L)
<i>AD4</i>	T_{mR}	Steering Motor Torque (R)
<i>AD5</i>	γ	Yaw Rate
<i>AD6</i>	a_y	Lateral Acceleration
<i>DA1</i>	T_L^*	Driving Torque Reference (L)
<i>DA2</i>	T_R^*	Driving Torque Reference (R)
<i>DA3</i>	T_{mL}^*	Steering Torque Reference (L)
<i>DA4</i>	T_{mR}^*	Steering Torque Reference (R)

where

δ_L : the steering angle of the left wheel;

δ_R : the steering angle of the right wheel;

T_{mL} : the torque output of the left steering motor; and

T_{mR} : the torque output of the right steering motor.

These equations can be transformed into a state space model, by putting:

$$\dot{\mathbf{x}} = \mathbf{A}\mathbf{x} + \mathbf{B}\mathbf{u} \quad (4.30)$$

$$\mathbf{y} = \mathbf{C}\mathbf{x} \quad (4.31)$$

where

$$\mathbf{x} = \begin{bmatrix} \delta_L \\ \delta_R \\ \dot{\delta}_L \\ \dot{\delta}_R \\ \beta \\ \gamma \end{bmatrix} \quad (4.32)$$

$$\mathbf{u} = \begin{bmatrix} T_{mL} \\ T_{mR} \\ M_z \end{bmatrix} \quad (4.33)$$

and

$$\mathbf{A} = \begin{bmatrix} 0 & 0 & 1 & 0 & 0 & 0 \\ 0 & 0 & 0 & 1 & 0 & 0 \\ -\frac{eC_f}{I_w} & 0 & 0 & 0 & \frac{eC_f}{I_w} & \frac{el_fC_f}{I_wV} \\ 0 & -\frac{eC_f}{I_w} & 0 & 0 & \frac{eC_f}{I_w} & \frac{el_fC_f}{I_wV} \\ 0 & 0 & 0 & 0 & \frac{2C_r}{mV} & -\frac{2l_rC_r}{mV^2} - 1 \\ 0 & 0 & 0 & 0 & -\frac{2l_rC_r}{I_z} & \frac{2l_r^2C_r}{I_zV} \end{bmatrix} \quad (4.34)$$

$$\mathbf{B} = \begin{bmatrix} 0 & 0 & 0 \\ 0 & 0 & 0 \\ \frac{1}{I_w} & 0 & 0 \\ 0 & \frac{1}{I_w} & 0 \\ \frac{1}{emV} & \frac{1}{emV} & 0 \\ \frac{l_f}{eI_z} & \frac{l_f}{eI_z} & \frac{1}{I_z} \end{bmatrix} \quad (4.35)$$

$$\mathbf{C} = \begin{bmatrix} 1 & 0 & 0 & 0 & 0 & 0 \\ 0 & 1 & 0 & 0 & 0 & 0 \\ 0 & 0 & 0 & 0 & 0 & 1 \end{bmatrix} \quad (4.36)$$

therefore

$$\mathbf{y} = \begin{bmatrix} \delta_L \\ \delta_R \\ \gamma \end{bmatrix} \quad (4.37)$$

where all parameters are from Table 4.1, and if not specified, from Table 3.1. From this state space model, the transfer functions $G_{\gamma T_{mL}}$, $G_{\gamma T_{mR}}$, and $G_{\gamma M_z}$ can be calculated. Let us define:

$$G_{\gamma T_{mL}} = \frac{E(s)}{F(s)} \quad (4.38)$$

$$G_{\gamma T_{mR}} = \frac{P(s)}{Q(s)} \quad (4.39)$$

$$G_{\gamma M_z} = \frac{R(s)}{S(s)} \quad (4.40)$$

4.4 System Analyses of CIMEV

Using equations (4.30)~(4.36), system stability and controllability are analyzed. These two are important engineering questions that lie at the heart of control using state space models, which determine whether we can steer the state via the control inputs to certain locations in the state space. Additionally, system behavior in response to the inputs is seen by transfer function analyses using equations (4.38)~(4.40).

4.4.1 Stability Analysis

The open-loop stability of the system can be seen by checking the eigenvalues of the matrix \mathbf{A} of (4.34). Substituting parameters into \mathbf{A} , and changing vehicle speed V gives us the result shown in Fig. 4.9. As seen in the figure, there always exists an unstable pole in the

right half plane regardless of vehicle speed. This unstable pole makes the system open-loop unstable, and consequently the system needs feedback control.

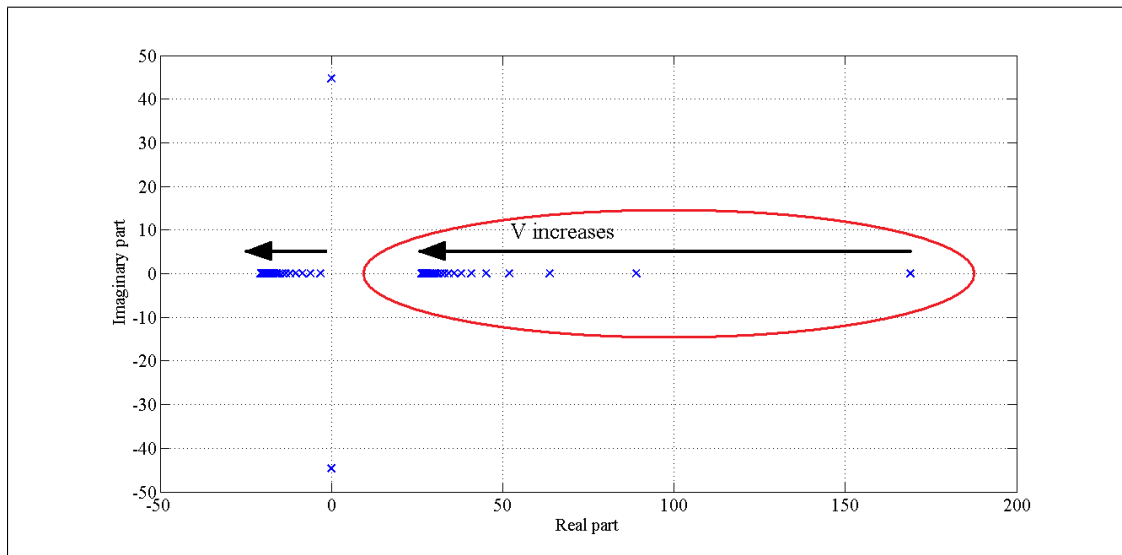


Figure 4.9: Eigenvalues of matrix \mathbf{A} : there always exists an unstable pole in the RHP (in the red circle), which makes the system open-loop unstable regardless of the vehicle speed V .

By the way, many modern engineering designs often have the open-loop unstable system in order to achieve high controllability or high mobility. For example, unlike the passenger airliners which are designed to be always open-loop stable, jet fighters usually have unstable plants which allow them to have high mobility and thus superior competence in aerial combats.

Also in case of CIMEV as far as the vehicle is controlled, it is provided with high mobility such as zero-radius turning, variable understeer gradient, and etc., which are shown later in this chapter. Prior to this, in order to see if the system is stabilizable, the controllability of the system is checked.



Figure 4.10: Modern engineering designs: an open-loop stable passenger airliner A380 on the left, and an unstable jet fighter F35 on the right [34][35].

4.4.2 Controllability Analysis

The idea of controllability covers stabilizability, i.e. if a system is completely controllable, it is implied that the system is always stabilizable. Also even in case that the system is not completely controllable, if its uncontrollable subspace is stable, the system is stabilizable [36]. Thus here the system controllability is analyzed using equations (4.30)~(4.36).

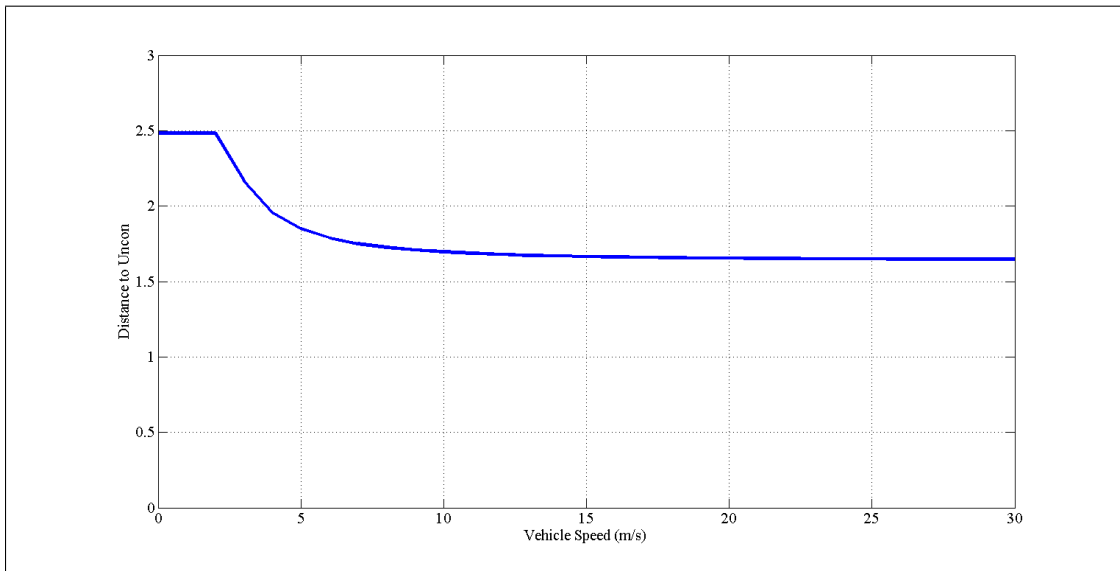


Figure 4.11: Relative controllability of the system with varying vehicle speed.

The controllability matrix $\Gamma_c[A, B]$, whose rank turns out to be full rank of 6, indicates that the system is completely controllable. From this result it is shown that the system can be always stabilizable. Furthermore, Fig. 4.11 shows the distance to the uncontrollability of the system, which is defined in (3.43) of Eising [27], when the vehicle speed is varying. The value is the highest when the vehicle speed is low, and as the speed increases the value drops. Note that the quantified controllability of the vehicle is higher than the values in Fig. 3.13, and Fig. 4.3. Considering that the distance tends to become smaller when the system dimension gets bigger [37], this result indirectly shows that CIMEV is better than the conventional ones in terms of robustness of control, and underpins our expectations of high mobility being given to the system. In order to achieve this, first of all, the controllers need to be designed properly, which is discussed in the following section.

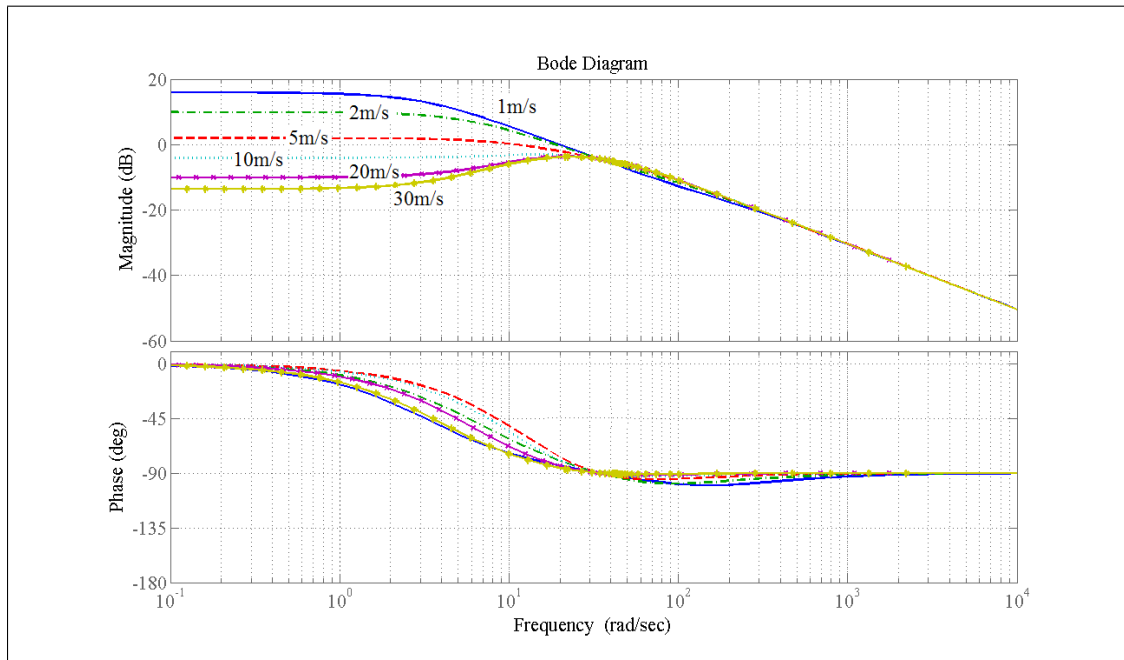


Figure 4.12: Bode Plot: Steering Torque Input vs. Vehicle Yaw Response

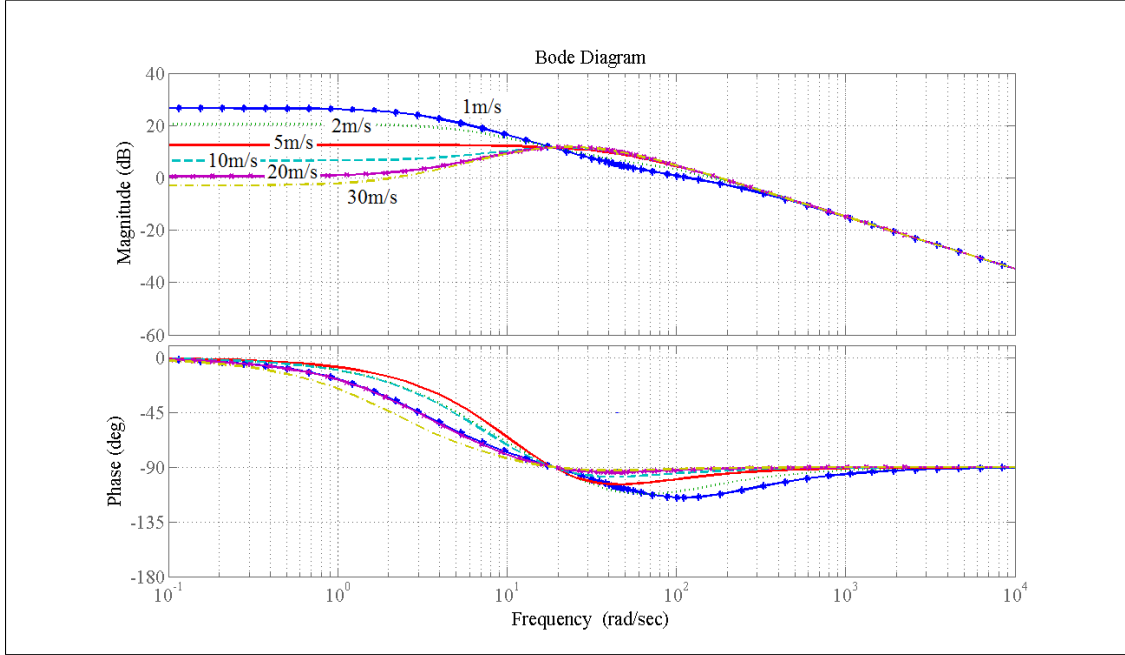


Figure 4.13: Bode Plot: Direct Yaw Moment Input vs. Vehicle Yaw Response

4.4.3 System Yaw Response

Figure 4.12 and 4.13 are bode diagrams of equations (4.38)~(4.40) which show the system yaw responses according to the steering torque input and the direct yaw moment input, respectively. It can be seen that the gain of the two inputs are well balanced, even larger when the direct yaw moment input is given, compared with Fig. 3.15 and 3.17, which means that we can effectively use the three inputs in total – two steering inputs and one direct yaw moment input – in two dimensional vehicle motion control.

It can be also seen that the gain decreases in accordance with increase in the vehicle speed. In general, vehicle needs a greater yaw rate at a higher vehicle speed for cornering, thus when the vehicle speed is high the steering angle needs to be controlled, not the torque, in order to achieve favorable yaw response, which is the case shown in Fig. 3.15. This implies that the control logic needs to be switched according to varying vehicle speed. With a strong position control of the steering angle, the response will converge on that of Fig. 3.15.

4.5 Controller Design

Based on the observations of the previous section, control strategies are developed in this section. Control logics in order to achieve high mobility and stability are discussed and verified by simulations and experiments.

The global control scheme for CIMEV is shown in Fig. 4.14. The upper-level controller computes the direct yaw moment reference and the lateral force reference in the form of the steering angles in order to meet the speed and yaw rate requirements. The lower-level controllers which are the driving controller and the steering controller, assign the motor torques to give the vehicle speed, yaw rate, and the steering angles.

The vehicle speed is directly calculated from two encoders (wheel speed sensors) attached to the driving wheels; the yaw rate is measured by the gyro sensor; and the steering

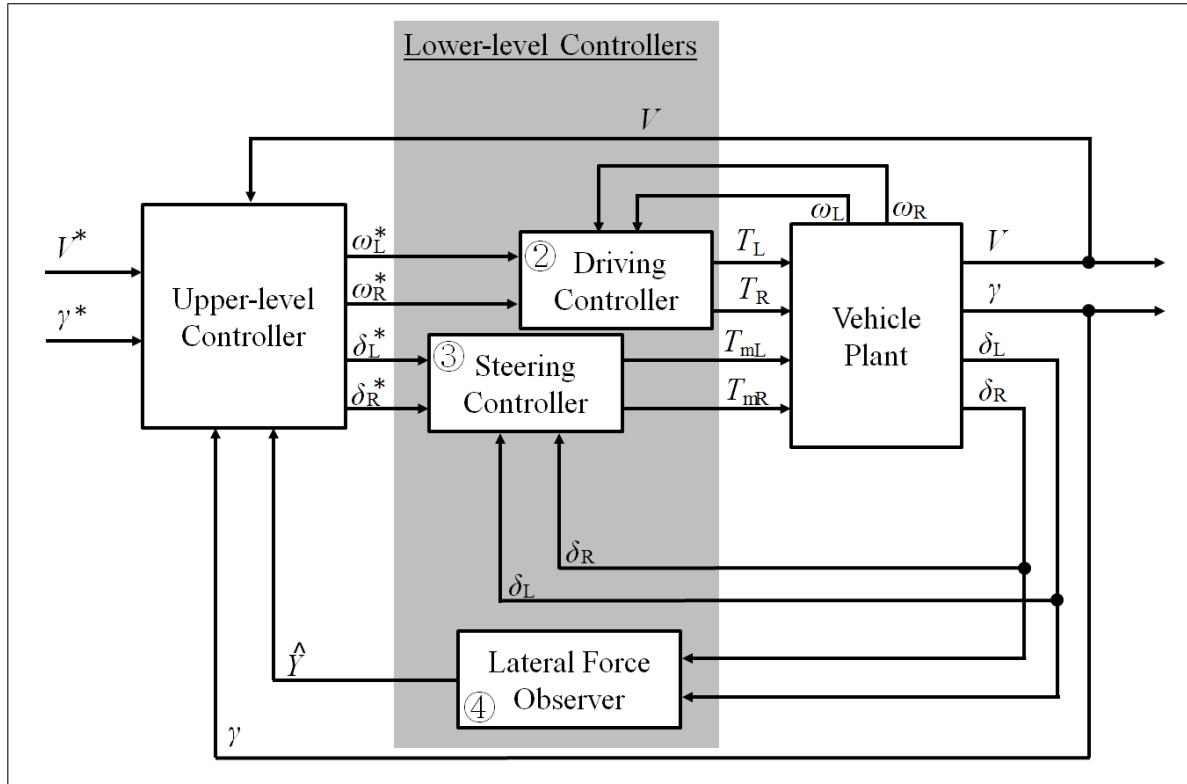


Figure 4.14: Block diagram of the global control scheme for CIMEV.

angles are measured by the two encoders (steering angle sensors) attached to the steering motors. It is assumed here that there is no longitudinal slip between the tire and the road surface.

4.5.1 Upper-level Controller

The upper-level controller, denoted as ① in Fig. 4.14, computes the desired direct yaw moment and desired steering angles, using the information of the vehicle speed reference and the yaw rate reference with feedback signals from the sensors.

The two references – vehicle speed and yaw rate – are given by the driver through the steering wheel, and the acceleration and brake pedals in passenger vehicle case. Meanwhile, they are given through the radio controller in CIMEV case. Using these references along with the feedback signals of the actual vehicle speed and the yaw rate from the wheel speed and gyro sensors, the references of the direct yaw moment in the form of the wheel speed and the steering angles are computed. Assuming a constant vehicle speed, and pursuing a zero vehicle side slip angle (i.e. $\beta^* = 0$), the process can be described as below. For the steering angle references, from equations (2.18), and (4.26)~(4.29), we can simply put:

$$\delta_L^* = \delta_R^* = \frac{L}{V^*} \gamma^* \quad (4.41)$$

$$M_z^* = I_z \frac{d}{dt} \gamma^* \quad (4.42)$$

and if we assume that the current controller of the motors are fast enough, then the driving speed references are given by the geometry shown in Fig. 2.7 as follows:

$$\frac{R(\omega_L + \omega_R)}{2} = V^* \quad (4.43)$$

$$R(\omega_R - \omega_L) = d\gamma^* \quad (4.44)$$

thus

$$\omega_L^* = \frac{2V^* - d\gamma^*}{2R} \quad (4.45)$$

$$\omega_R^* = \frac{2V^* + d\gamma^*}{2R} \quad (4.46)$$

These reference values are applied when the vehicle speed is low, i.e. the steering control is disabled.

Yet in addition to this, in order to minimize the tire side slip, which causes the cornering resistance and the consequent mechanical loss, and to maintain the linearity of the steering characteristics regardless of the vehicle speed, the estimated lateral force \hat{Y} is compensated by the direct yaw moment at a high speed. Thus the wheel speed references are:

$$\omega_L^* = \frac{2V^* - d\gamma^*}{2R} - C_{lat}\hat{Y} \quad (4.47)$$

$$\omega_R^* = \frac{2V^* + d\gamma^*}{2R} + C_{lat}\hat{Y} \quad (4.48)$$

where C_{lat} is the lateral force compensator gain.

4.5.2 Driving Controller

The driving controller, denoted as ② in Fig. 4.14, provides two driving torque outputs which assign the vehicle the traction forces and the direct yaw moment based on the information given by the upper-level controller. It consists of two speed and torque (current) controlled DC motors, where the two-degree-of-freedom (2DOF) control method is used in order to achieve fast response and fair robustness. The block diagram of the driving controller is shown in Fig. 4.15.

The feedback and feed forward gains are set as:

$$C_{FF}(s) = \frac{0.05s + 1}{2.68} \quad (4.49)$$

$$C_{FB}(s) = 1 \quad (4.50)$$

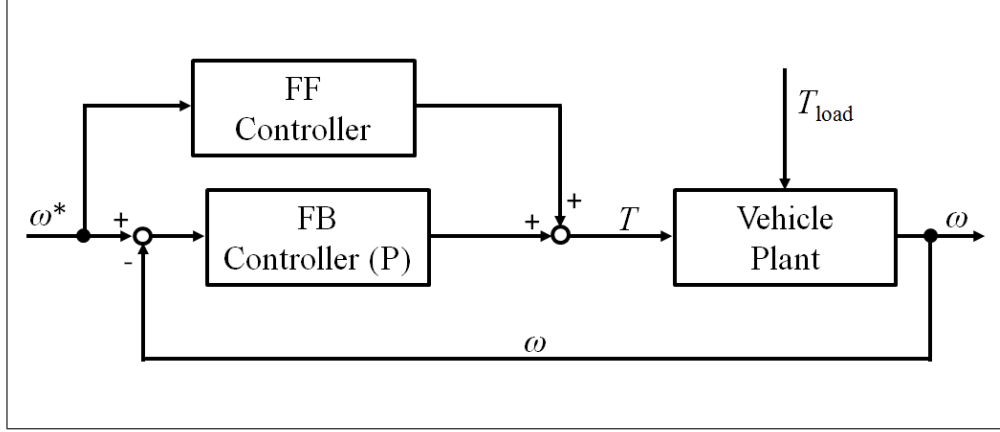


Figure 4.15: Driving motor controller.

by inverting the approximated plant dynamics. The torque transmission is done through the timing belts. Thus if the feedback gain is too high, the belts break. Empirically, it is found that the belts are easy to break when the gain is set over 2. The feed forward gain is set as the inverse model of the plant.

4.5.3 Steering Controller and Lateral Force Observer

The steering controller, denoted as ③ in Fig. 4.14, controls the two steering angles using the two-degree-of-freedom (2DOF) position control loop and the disturbance observer. This controller plays the most important roll in the proposed system by providing the estimated lateral force information to the entire system. The estimated disturbance torque is used to compensate the disturbance itself within the loop, and transmitted to the upper-level controller at the same time.

The block diagram of the steering controller is shown in Fig. 4.16. The feed forward controller is designed based on the inverse plant model, which is given by:

$$C_{FF}(s) = P(s)^{-1} = \frac{s(s+2)}{72} \quad (4.51)$$

and the feedback gain is given as:

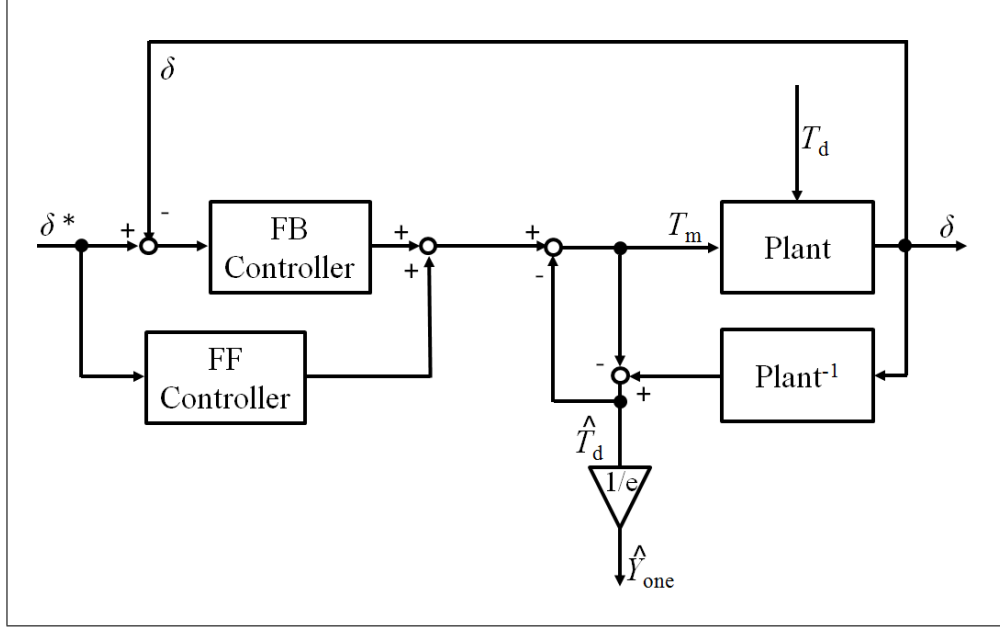


Figure 4.16: Steering motor controller.

$$C_{FB}(s) = 5 \quad (4.52)$$

by inverting the approximated plant dynamics.

The lateral force observer, denoted as ④ in Fig. 4.14, is a part of the steering controller. The estimated disturbance torque in Fig. 4.16 is simply converted into the estimated lateral force as divided by the caster length e , assuming that the dominant part of the disturbance torque is the lateral force. This information is fed back to the upper-level controller helping to decide the reference values.

4.5.4 Speed Range and Control Mode

In a low speed range, the steering motors do not need to work actively, i.e. only with the direct yaw moment input and passive caster wheels, the vehicle movement can be managed satisfactorily as observed in the previous subsection. Moreover, active steering can even

cause loss of energy during cornering owing to the tire slip and the consequent cornering resistance of the wheels [38].

On the other hand, at a high vehicle speed, tires need to produce lateral forces in order to maintain a turn. These lateral forces are crucial because they provide the vehicle with the centripetal force during cornering. Thus the steering motors should be actively controlled for safety and stability reasons.

Consequently the control mode has to be switched in accordance with the vehicle speed change. However determining the threshold speed is not a simple process. Many factors need to be considered, which is out of the scope of this thesis, and is a part of the future works. Here in this work, it is assumed that in a reasonably low speed range the steering control is disabled, and for a high speed range the steering control is on.

4.6 Experiment Results and Advantages of CIMEV

Using the controllers designed in the previous section, some experiments are done to show the advantages of the proposed system. In this section, the experiment results are introduced, and the corresponding advantages of the system are discussed.

4.6.1 High Mobility at Low Speed

Fig. 4.17 shows the experimental result of the vehicle yaw rate responses to the direct yaw moment input versus the conventional steering maneuver at 90 degrees cornering at a low speed of $1m/s$. For the conventional steering case, the steering angle was given by Ackermann geometry at 30 degrees which is usually the maximum for passenger vehicles. The control inputs are given by equations (4.41), (4.45), and (4.46).

It is shown that the yaw rate can go over the maximum rate of the conventional one at a given speed, by applying direct yaw moment to the driving wheels without causing any energy loss from cornering resistance, which corresponds the observation results from the system analyses. This property enables CIMEV to make a more sharp turn than a

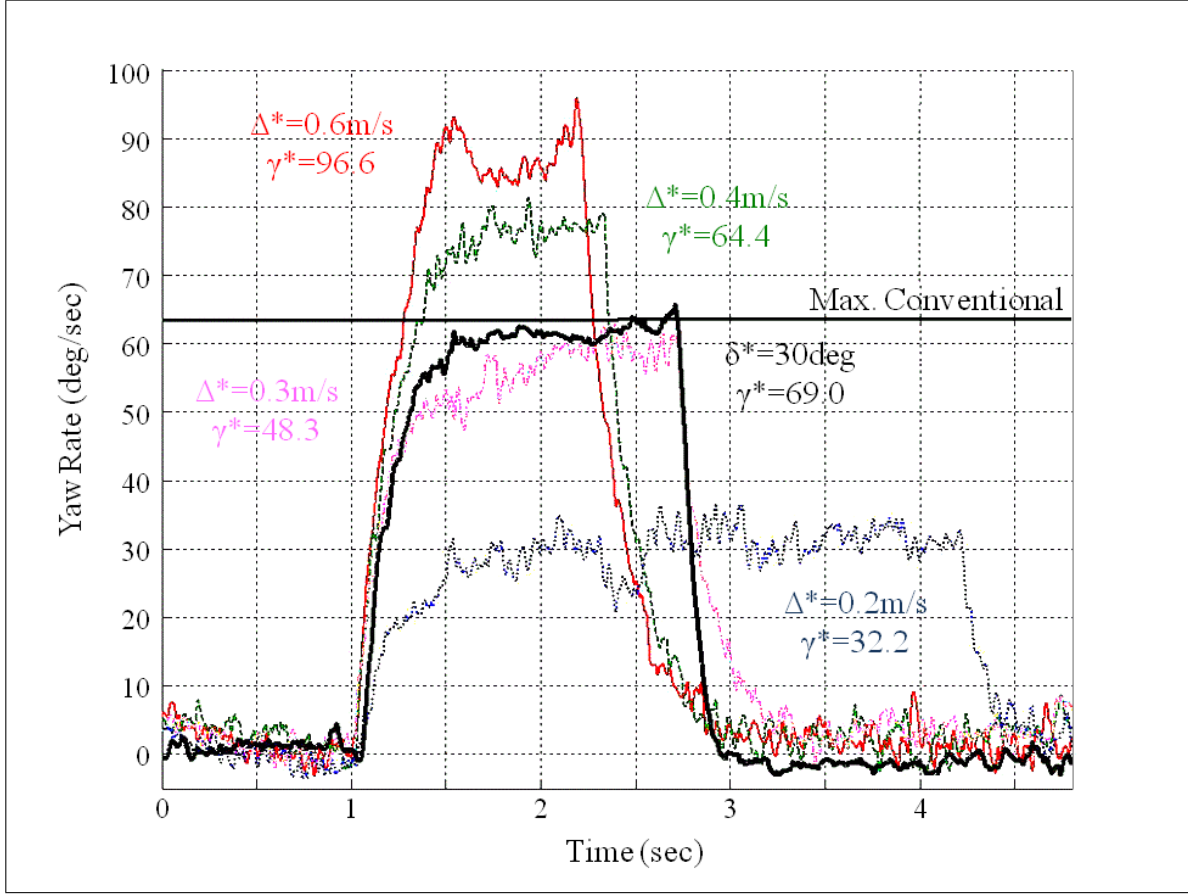


Figure 4.17: Yaw rate responses to the direct yaw moment input versus the conventional steering maneuver at 90 degrees cornering. Vehicle speed is 1m/s in all cases. The steering angle is 30 degrees at inner wheel for the conventional steering case. Direct yaw moment is given by wheel speed controller.

conventionally steered vehicle does, so that CIMEV can move more freely in restricted spaces. This experiment result also can be associated with the ICR location shown in Fig. 4.18. Usually a normal passenger vehicle has the minimum turning radius of 5 meters, meanwhile CIMEV can turn with zero radius.

At low speed, the advantage of using caster wheels is obvious: as the way they are defined, they freely rotate and so does the vehicle. Vehicles with the normal steering system, need to run in order to make turns. CIMEV, on the other hand, can make turns at

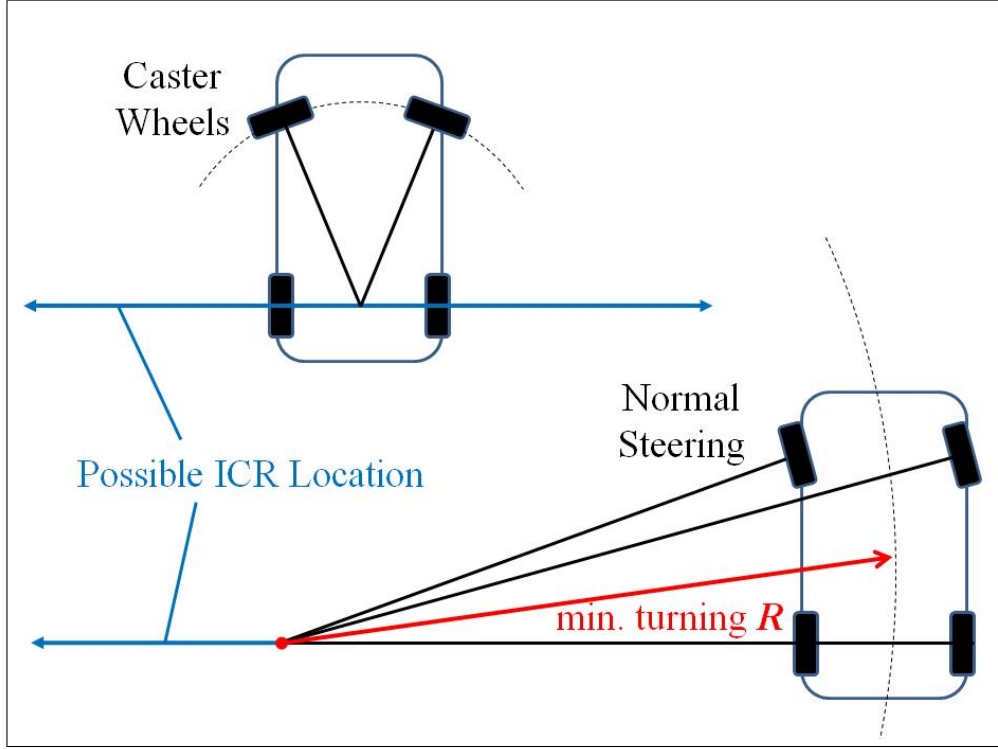


Figure 4.18: Possible location of ICR (Instant Center of Rotation), colored blue. CIMEV (upper) and conventional one (lower). Vehicle with normal steering has usually 5 meters of minimum turning radius, while CIMEV has zero at zero vehicle speed.

speed of zero. This property is advantageous not only for the passenger EV applications, but also for the vehicles or the mobile robots which work in restricted spaces.

Note that, as it can be seen in Fig. 4.17, the yaw rate tends to have higher response over the given reference value when the vehicle is moment steered. This can be explained by the fact that the inertia to be controlled is much larger in the direct yaw moment steer case than the opponent.

4.6.2 Making Use of Lateral Force Observer

Since CIMEV is equipped with two independent steering motors, it is possible to apply disturbance observers [39] in the control logic of each wheel. From equations (4.26) and

(4.27), if we define the disturbance torques for the left and right as:

$$T_{dL} = eC_f\beta + \frac{el_fC_f}{V}\gamma - eC_f\delta_L = eC_f\alpha_L \simeq eY_L \quad (4.53)$$

$$T_{dR} = eC_f\beta + \frac{el_fC_f}{V}\gamma - eC_f\delta_R = eC_f\alpha_R \simeq eY_R \quad (4.54)$$

the lateral force can be simply calculated by dividing the caster length e without using any special sensors to measure it, and moreover, by controlling the steering angles, the vehicle is allowed to have the controlled lateral forces, which gives a lot of implications to vehicle motion control field.

Lateral Force Observer Verification

Fig. 4.19 compares the lateral forces between the one calculated by using disturbance observers and by using acceleration sensor. Since it is a steady state circle running condition (i.e. $\dot{\gamma} = 0$ and $M_z = 0$), using equations (4.26)~(4.29), disturbance torques were converted into lateral forces (red and blue dashed lines), and the lateral acceleration was converted into the necessary net lateral force to make the turn (black solid line). Experimental result shows that the lateral force estimation by using disturbance observer has reliable accuracy although it has some offset, as compared with the calculation using acceleration sensor. For better accuracy of the estimation method, the offset and its implications need to be further investigated.

Discussion on Load Transfer

As seen in Fig. 4.19, the outer wheel has larger value in the estimated lateral force than the inner one. In this thesis, it is assumed that the cornering stiffness C_f has a fixed value, however, in reality the value changes due to the dynamic change in vertical load. It is found, from the experimental result and from the definition of C_f in 2.2.2, that the ratio of the vertical load is around 0.63 between the inner and outer wheels.

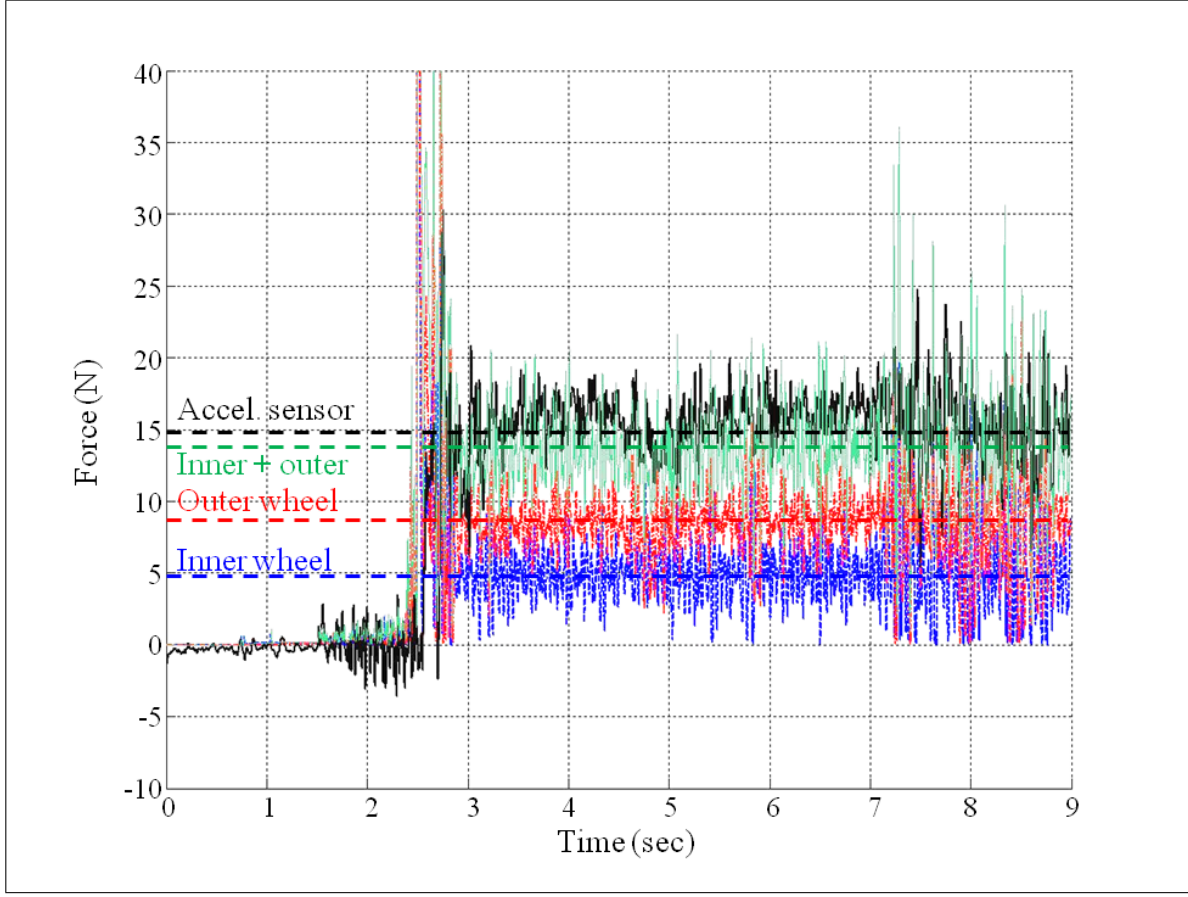


Figure 4.19: Lateral forces calculated by using disturbance observer versus the one calculated by using lateral acceleration sensor during a steady state circle running. Vehicle speed was $2m/s$, and the steering angle was 15 degrees at inner wheel.

On the other hand, from the experiment condition, and the vehicle geometry and parameters, for a given lateral acceleration, the vertical load of the front wheels can be roughly calculated as:

$$N_{zFL} = 39.2 + 3.6a_y \quad (4.55)$$

$$N_{zFR} = 39.2 - 3.6a_y \quad (4.56)$$

where, a_y of this experiment was $1.87m/s^2$, thus the ratio N_{zFL}/N_{zFR} should be around

0.69, which is fairly close to the value from the experiment result. This observation implies that, by using the lateral force observer, the dynamic load transfer of a running vehicle can be calculated without attaching any special sensors such as a potentiometer. More investigation needs to be done for better accuracy.

Understeer Gradient Control

Furthermore, it is also possible at a high vehicle speed to change the understeer characteristics by using the lateral force feedback control. Let us call it the understeer gradient control. The understeer gradient K_{us} is one of the major vehicle dynamic characteristics during cornering, which is introduced in 2.3.2.

CIMEV inherently is a severely understeered vehicle due to the free rotation of the casters, however, by using this control it becomes close to a neutral steered one. The understeer gradient controller makes α_f smaller by giving the positive feedback of the estimated lateral force \hat{Y} to the direct yaw moment M_z , and thus it virtually makes the cornering stiffness C_f larger: refer to equation (2.16). Consequently K_{us} can be controlled to go closer to zero. The control scheme is shown in Fig. 4.20, and the experimental results are shown in Fig. 4.21 and 4.22. The vehicle ran on a circle and was accelerated from 0 to 4 m/s.

Usually a passenger vehicle is an understeered one, and has a peak in yaw rate gain

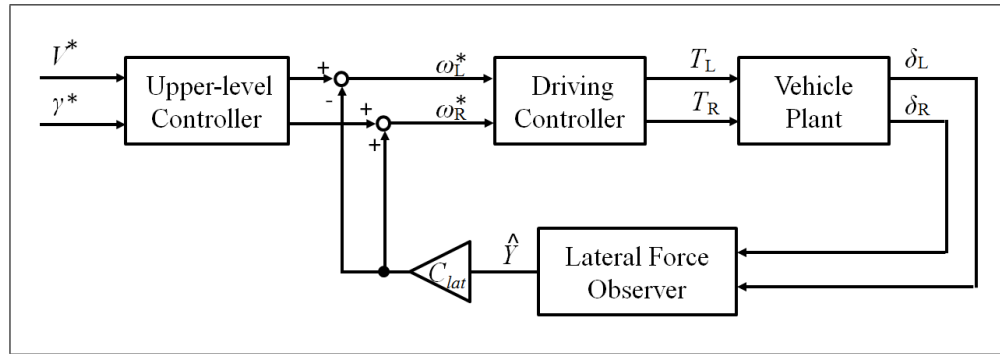


Figure 4.20: Understeer gradient controller.

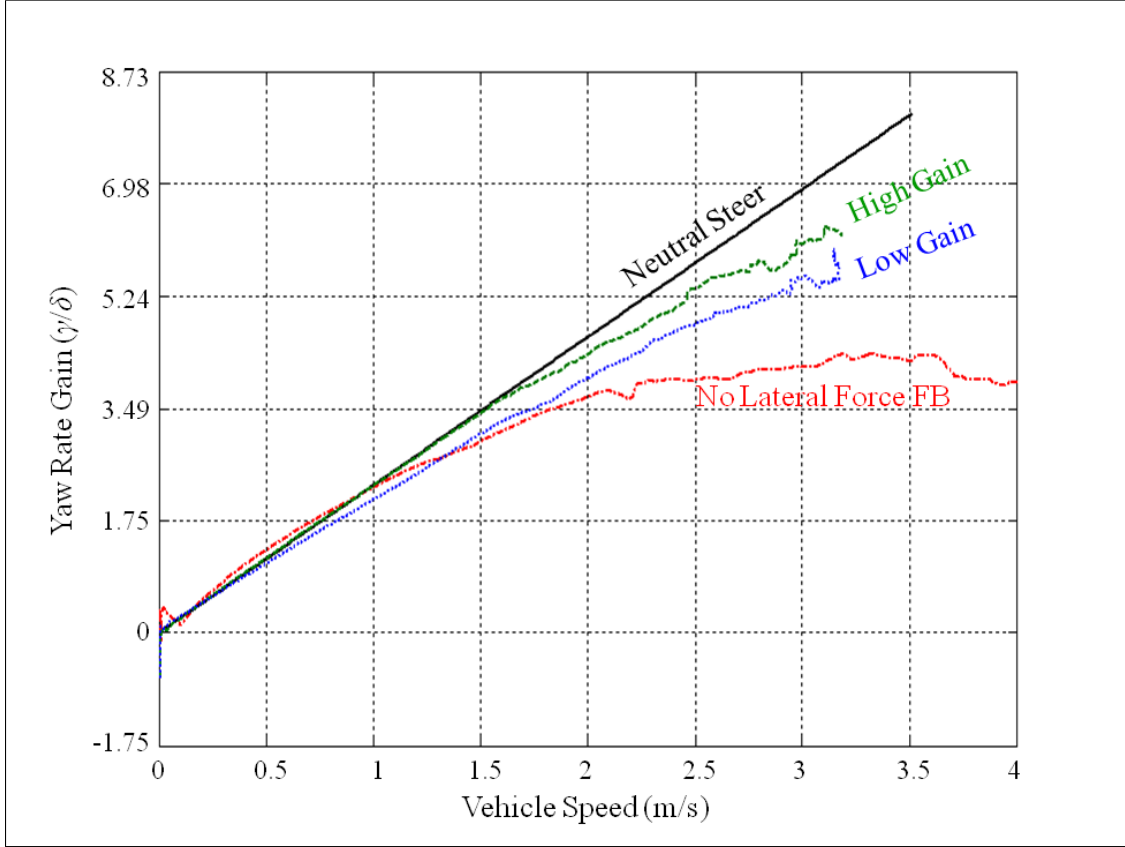


Figure 4.21: Understeer gradient control: Change in slope (understeer gradient K_{us}).

at a certain vehicle speed – the characteristic speed V_{char} , like the red dotted case in Fig. 4.21 and 4.22, so the radius of cornering gets bigger as the vehicle accelerates. On the other hand, the neutral steered vehicle can run on a circle of a constant radius regardless of its speed, which gives the driver a natural (linear) feeling during cornering. By using the understeer gradient control, the cornering characteristics of CIMEV can be tuned to the driver's favor, i.e. the value can be controlled by changing the gain C_{lat} as shown in Fig. 4.21.

Bank Angle Estimation

Another advantage of using the lateral force observer is the estimation of the road bank angle on which the vehicle is running. It is based on a simple kinematic relation between the

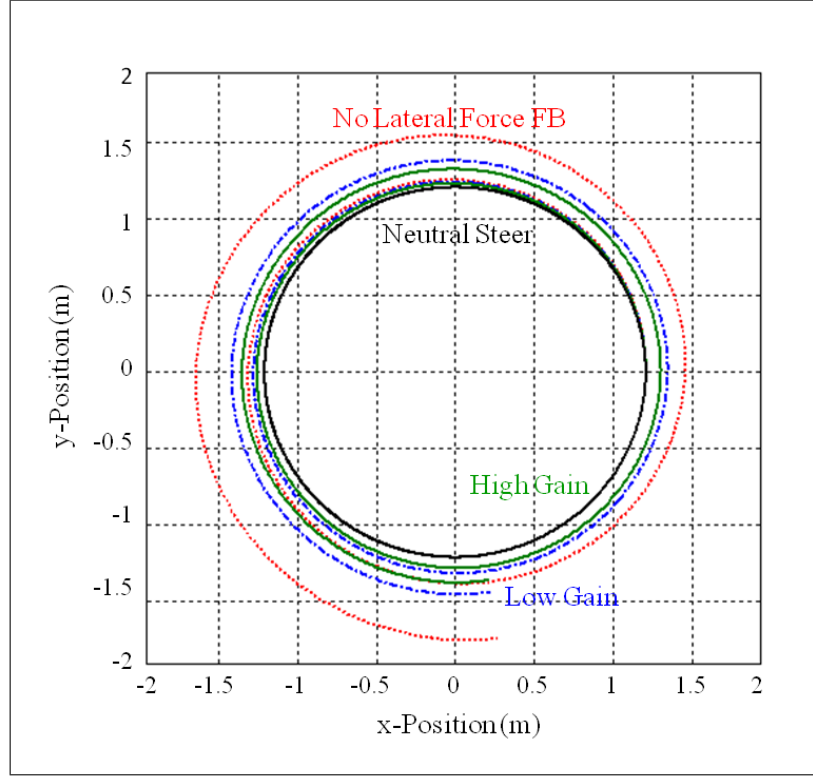


Figure 4.22: Understeer gradient control: Vehicle trajectory during an accelerating circle run.

gravitational force and the lateral force of the front wheels as shown in Fig. 4.23 without using any special sensors. When a vehicle is running straight on a road which has a bank angle of φ , from the kinematic relation it is written as:

$$\hat{Y} = \frac{l_r}{L} mg \sin \varphi \quad (4.57)$$

thus φ can be estimated as:

$$\hat{\varphi} = \sin^{-1} \frac{\hat{Y}L}{l_r mg} \simeq \frac{\hat{Y}L}{l_r mg} \quad (4.58)$$

It can be seen in the Fig. 4.25 that the two lateral acceleration signals agree well, and the estimated and measured values are acceptable. The bank angle of the road is 10.5 degrees, which assigns $1.79m/s^2$ of lateral acceleration due to gravity. The vehicle was

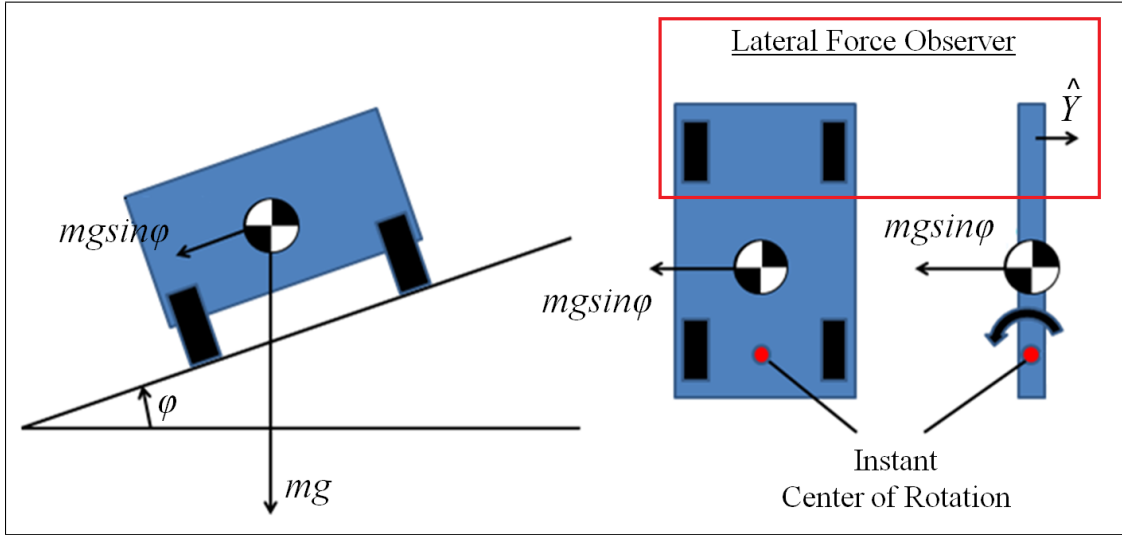


Figure 4.23: Kinematic Relations of Bank Angle Estimation.



Figure 4.24: Bank where the experiment was carried out. The bank angle is 10.5 degrees.

released at $t = 2$ by hand, and the vehicle speed increases upto $2m/s$. As the vehicle starts to run, the lateral force observer works properly.

It is a simple and cost effective method, however in order to apply this method in a passenger vehicle application, decoupling the effects of the bank angle and the lateral acceleration during cornering needs to be investigated.

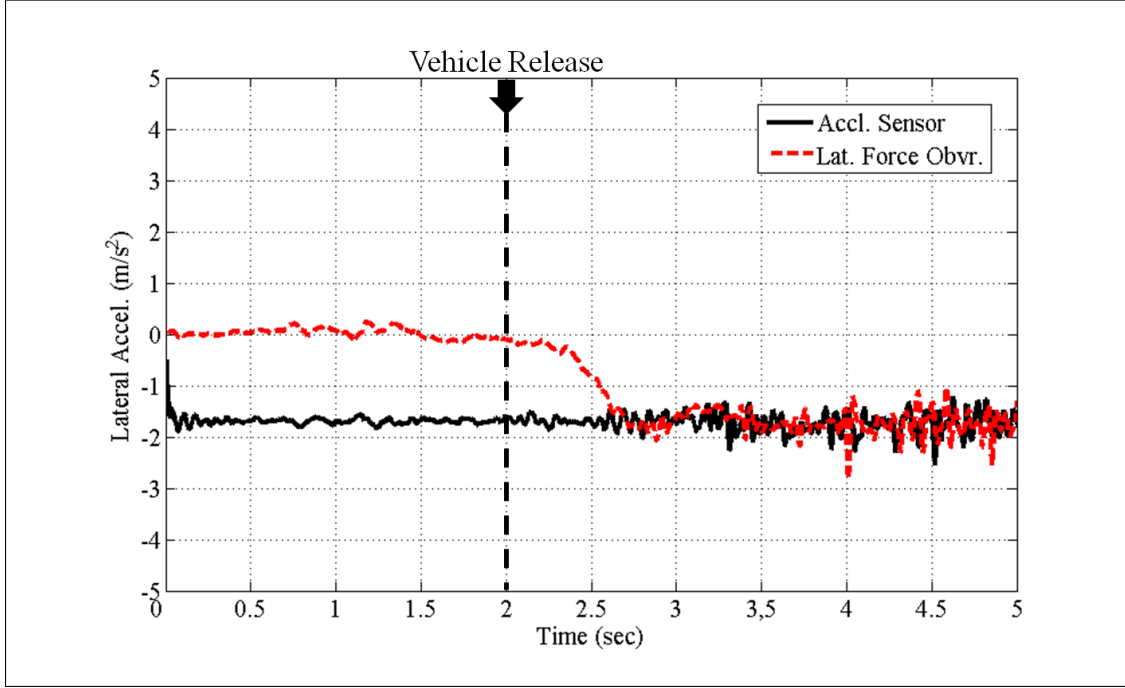


Figure 4.25: Lateral acceleration signal from the acceleration sensor and the lateral force observer. Vehicle is released at $t = 2$, and the vehicle speed increases upto $2m/s$.

4.7 Summary

In this chapter, a novel chassis structure for electric vehicles is proposed using caster wheels and independent driving motors. An actual experimental vehicle is introduced, and its system configuration is shown. The mathematical model is discussed with simulations, and the system stability is analyzed. Feasibility and the advantages of the system is shown with experiment results.

From observations made in this chapter, it is clear that the proposed system has following advantages compared with the conventional system:

- The open-loop system is unstable, however the system is completely controllable and the relative controllability seems to be higher than that of the conventional vehicles, which is implied indirectly.

- The yaw gains of the inputs – the steering and the direct yaw moment, are well balanced which makes the system effectively controlled.
- At low speed, CIMEV shows high mobility. It is applicable in various fields such as passenger EVs, mobile robots, military and space rovers which work in limited spaces.
- Utilizing lateral force observer, the lateral force during cornering can be estimated and possibly controlled. By doing this it is possible to reduce energy loss from the cornering resistance, or to control the characteristics of the vehicle such as the understeer gradient.

Chapter 5

Concluding Remarks

5.1 Significance of the Result

This work was motivated by the fact that the vehicle electrification does not mean only the change in power source of the vehicle, but the vehicle chassis structure itself can be changed. Despite the underlying importance, however, it seems that there has been no attempt to provide an appropriate and unique structure for the independent motor driven EVs.

In this work, followed by the studies on wheel placements and their effects on the vehicle behavior, a novel chassis structure using caster wheels and independent driving motors is proposed. Provided with four wheels the system is designed to be statically stable, and with caster wheels on the front axle the proposed system is able to use the two kinds inputs – the steering and the direct yaw moment – effectively for two-dimensional motion control. The consequent unique advantages of the system are shown with experimental results.

Considering the advantages shown in this work, the proposed system could be an attractive alternative for the future EV's structure for better dynamic performances. Yet, there still remain some problems to clear before the practical application of the proposed system.

5.2 Future Works

First of all, the problem shifts to the safety issues. The proposed system is inherently unstable, and thus the system always needs to be actively controlled. The electronically

controlled systems, however, are always in doubt about failure. For example, the steer-by-wire systems are currently not allowed to use for passenger vehicles. Instead, the whole parts of the steering system must be mechanically connected for safety reasons. Likewise for practical application of the novel system, the fail-safe logics must be thoroughly designed.

Secondly, this thesis ends with the proposal of a novel structure, and the introduction of some of its unique characteristics. So there are many things left to do. As the electric motor can be placed anywhere within the vehicle, a number of variations in vehicle structure can be realized, and of course the control strategies vary according to the variation in structure. Through further studies on wheel placements and the corresponding vehicle dynamics, many other challenges need to be made.

Finally, this work was done limiting the assumption to the passenger vehicle applications. However, there are many other possible forms of electric vehicle such as mobile robots, space rovers, and combat robots. Each of these applications has different requirements and its unique perspectives. Thus more works need to be done for adapting the system to various applications, considering the specific requirements. And the other way around, to find a suitable application for the proposed system can be also an interesting engineering work.

References

- [1] <http://mikes.railhistory.railfan.net>
- [2] <http://inventors.about.com>
- [3] <http://www.cgl.uwaterloo.ca/~racowan/escape.html>
- [4] http://ec.europa.eu/transport/urban/vehicles/road/electric_en.htm
- [5] A. R. Holdway, A. R. Williams, O. R. Inderwildi, and D. A. King, "Indirect emissions from electric vehicles: emissions from electricity generation," *Energy Environmental Science*, Vol. 3, No. 12, pp. 1825, 2010
- [6] S. M. Lukic, R. C. Bansal, and A. Emadi, "Energy Storage Systems for Automotive Applications," *IEEE Transactions on Industrial Electronics*, Vol. 55, No. 6, 2008
- [7] J. Huh, E. Park, G. Jung, and C. Rim, "High Efficient Inductive Power Supply System Implemented for On Line Electric Vehicles," *KIPE Autumn Conference 2009 Proceedings*, pp. 105-110, 2009
- [8] T. Imura, H. Okabe, and Y. Hori, "Basic experimental study on helical antennas of wireless power transfer for Electric Vehicles by using magnetic resonant couplings," *IEEE Vehicle Power and Propulsion Conference Proceedings*, 2009
- [9] Y. Hori, "Future Vehicle Driven by Electricity and Control – Research on Four-Wheel-Motored 'UOT Electric March II'," *IEEE Transactions on Industrial Electronics*, Vol. 51, No. 5, pp. 954-962, 2004
- [10] D. Yin and Y. Hori, "A new approach to traction control of EV based on maximum effective torque estimation," *Proceedings of the 34th Annual Conference of the IEEE Industrial Electronics Society*, pp. 2764-2769, 2008

- [11] K. Kawashima, T. Uchida, M. Tomizuka, and Y. Hori, "Rolling stability control of in-wheel electric vehicle based on two-degree-of-freedom control," *The 10th IEEE International Workshop on Advanced Motion Control*, pp. 751-756, 2008
- [12] T. D. Gillespie, "Fundamentals of Vehicle Dynamics," *Society of Automotive Engineers*, Warrendale, PA
- [13] M. Abe, "Automotive Vehicle Dynamics, Theory and Applications," *TDU Press*, 2008
- [14] "Vehicle Dynamics and Terminology," SAE J670e, *Society of Automotive Engineers*, Warrendale, PA
- [15] R. T. Bundorf "The Influence of Vehicle Design Parameters on Characteristic Speed and Understeer," SAE Paper No. 670078, *Society of Automotive Engineers*, pp. 14, 1976
- [16] H. Lee, S. Ryu, and J. Lee, "Optimal posture of Mobile Inverted Pendulum using a single gyroscope and tilt sensor," *ICROS-SICE International Joint Conference Proceedings*, 2009
- [17] Y. Kim, S. Kim, and Y. Kwak, "Dynamic Analysis of a Nonholonomic Two-Wheeled Inverted Pendulum Robot," *Journal of Intelligent and Robotic Systems*, Vol. 44, pp. 25-46, 2005
- [18] J. C. Huston, B. J. Graves, and D. B. Johnson, "Three Wheel Vehicle Dynamics," *SAE Transaction*, Vol. 91, No. 820139, 1982
- [19] NHTSA Vehicle Research and Test Center, "NHTSA Rollover Research," 2005
- [20] S. C. Peters and K. Iagnemma, "An Analysis of Rollover Stability Measurement for High-Speed Mobile Robots," *IEEE International Conference on Robotics and Automation Proceedings*, 2006

- [21] A. Hac, "Rollover stability index including effects of suspension design," *SAE Transaction*, No. 2002-01-0965, 2002
- [22] D. Odenthal, T. Bunte, and J. Ackerman, "Nonlinear steering and braking control for vehicle rollover avoidance," *European Control Conference Proceedings*, 1999
- [23] D. A. Messuri and C. A. Klein, "Automatic body regulation for maintaining stability of a legged vehicle during rough-terrain locomotion," *IEEE Journal Robotics and Automation*, Vol. RA-1, pp. 132-141, 1985
- [24] A. G. Nalecz, Z. Lu, and K. L. d'Entremont, "An Investigation into Dynamic Measures of Vehicle Rollover Propensity," *SAE Transaction*, No. 930831, 1993
- [25] E. Papadopoulos and D. Rey, "A new measure of tip over stability margin for mobile base manipulators," *IEEE International Conference on Robotics and Automation Proceedings*, pp. 3111-3116, 1996
- [26] C. Lee and T. Lee, "Stability Analysis of Three and Four Wheel Vehicles," *JSME International Journal*, Vol. 33, No. 4 1990
- [27] R. Eising, "Between controllable and uncontrollable," *Systems and Control Letters*, No. 4, pp. 263-264, 1984
- [28] <http://www.advancecaster.com>
- [29] S. Oh, and Y. Hori, "Development of Extended Wheelchair Operation to Estimate Precise Two-Dimensional Tilt Information ," *Proceedings of 2007 IDETC/CIE*, 2007
- [30] G. Somieski, "Shimmy Analysis of a Simple Aircraft Nose Landing Gear Model Using Different Mathematical Methods," *Journal of Aerospace Science and Technology*, No. 8, pp. 545-555, 1997

- [31] H. B. Pacejka, "Modelling of the pneumatic tire and its impact on vehicle dynamics behavior," Lecture Series DR 6.04, Carl-Cranz-Gesellschaft e.V., Oberpfaffenhofen, 1992
- [32] E. Bakker, L. Nyborg, and H. B. Pacejka, "Tyre modeling for use in vehicle dynamics studies," *SAE Paper*, No. 870421, 1987
- [33] D. de Falco, G. di Massa, and S. Pagano, "On the Castor Dynamic Behavior," *Journal of the Franklin Institute*, Vol. 347, pp. 116-129, 2010
- [34] <http://www.airbus.com>
- [35] <http://www.lockheedmartin.com>
- [36] G. C. Goodwin, "Control System Design," *Prentice Hall*, pp. 498, 2001
- [37] R. Eising, "The Distance between a System and the Set of Uncontrollable Systems," *Lecture Notes in Control and Information Sciences*, Volume 58, pp. 303-314, 1984
- [38] H. Sumiya and H. Fujimoto, "Proposal of Distribution Method of Front/Rear Wheel Side-Slip Angle and Left/Right Motor Torque for Range Extension Control System of Electric Vehicle," *IIC 2011 Proceedings*, 2011 (Japanese)
- [39] S. Komada, M. Ishida, K. Ohnishi, and T. Hori, "Disturbance Observer-based Motion Control of Direct Drive Motors," *IEEE Transactions on Energy Conversion*, Vol. 6, No. 3, 1991

Curriculum Vitae

Yunha Kim was born in Seoul, Korea on March 2, 1981. He received B.S. degree in Mechanical Engineering from Seoul National University in the spring of 2007. After graduation he entered the Technical Center, Renault Samsung Motors, Co., Ltd., where he had worked as an Engine Management System design engineer for two years until the spring of 2009.

In the fall of 2009, he entered the Graduate School of the University of Tokyo in pursuit of the Master's Degree in Electrical Engineering. His research interests include power electronics, robotics, and vehicle motion control.

Permanent address: Hillstate 112-404, Samseong 2-dong,
Gangnam-gu, Seoul, 135-092 Korea